minerals

MDPI

Article

Tectono-Metamorphic Evolution of Serpentinites from Lanzo Valleys Subduction Complex (Piemonte—Sesia-Lanzo Zone Boundary, Western Italian Alps)

Matteo Assanelli [1], Pietro Luoni [1], Gisella Rebay [2], Manuel Roda [1,*] and Maria Iole Spalla [1]

[1] Dipartimento di Scienze della Terra "A. Desio", Universitá degli Studi di Milano, 20133 Milano, Italy; matteo.assanelli@studenti.unimi.it (M.A.); pietro.luoni@unimi.it (P.L.); iole.spalla@unimi.it (M.I.S.)

[2] Dipartimento di Scienze della Terra e dell'Ambiente, Universitá degli Studi di Pavia, 27100 Pavia, Italy; gisella.rebay@unipv.it

* Correspondence: manuel.roda@unimi.it

Received: 23 September 2020; Accepted: 2 November 2020; Published: 5 November 2020

Abstract: In the upper Tesso Valley the folded contact between Piemonte Zone ophiolites and Sesia-Lanzo Zone continental crust is exposed. Here serpentinites, metabasites, calcschists and fine-grained gneisses are deformed by four ductile superposed groups of structures, associated with different mineral assemblages. Different serpentinite lithologies have been recognized and studied in detail. Mylonitic D2 structures are pervasive and mineral assemblages point to re-equilibration at T of 450 ± 50 °C and P of 0.8 ± 0.3 GPa, under blueschist/epidote amphibolite-facies conditions. Pre-D2 structures and mineral assemblages are relics within S2 and indicate a re-equilibration under eclogite-facies conditions, at T of 570 ± 50 °C and P > 1.8 GPa. Post-D2 occurs under greenschist-facies conditions. Numerical modeling of a subduction zone allows exploration of the geodynamic context in which such PT path could have developed, and to make hypotheses about the possible timing of such a scenario, in agreement with the timing generally proposed for the Alpine subduction and collision. Model predictions indicate that pre-D2 mineral assemblages may have developed during Paleocene at 60–90 km depth and 115–145 km from the trench, or, alternatively, during lower Eocene at ca. 70–90 km depth, and 135–160 km from the trench.

Keywords: eclogitized serpentinites; Ti-clinohumite; Alpine subduction; multi-scale structural analysis

1. Introduction

The Piemonte Zone of the Western Alps comprises the ophiolitic remnants of the Ligurian-Piedmont Ocean, dismembered by the polyphase tectono-metamorphic evolution recorded during the Alpine convergence e.g., [1–8]. Even though some authors consider the ophiolites of the Piemonte zone as lithospheric fragments of a magma-poor ocean-continent transition zone of the Tethys e.g., [9–11], they are widely interpreted as derived from the Ligurian-Piedmont oceanic lithosphere, [7] and refs. therein, since they have chemical, structural and lithostratigraphic characters similar to those of a subduction-unrelated oceanic lithosphere [12].

At the boundary between the Piemonte Zone (PZ) metaophiolites and the Austroalpine continental crust (Figure 1a,b), a tectonic mixing of thin slivers of calcschists, quartzites, metabasites, serpentinites and fine-grained gneisses (metapelites and metagranitoids) occurs all along the western margin of the central and southern Sesia-Lanzo Zone (SLZ), extending over a distance of 50 km, from Santanel

klippe to Lanzo Massif [13–16]. This portion of PZ, deeply entwined with the SLZ continental crust, shows heterogeneous metamorphic evolutions with climax conditions ranging from greenschist- to eclogite-facies conditions [13,15,17].

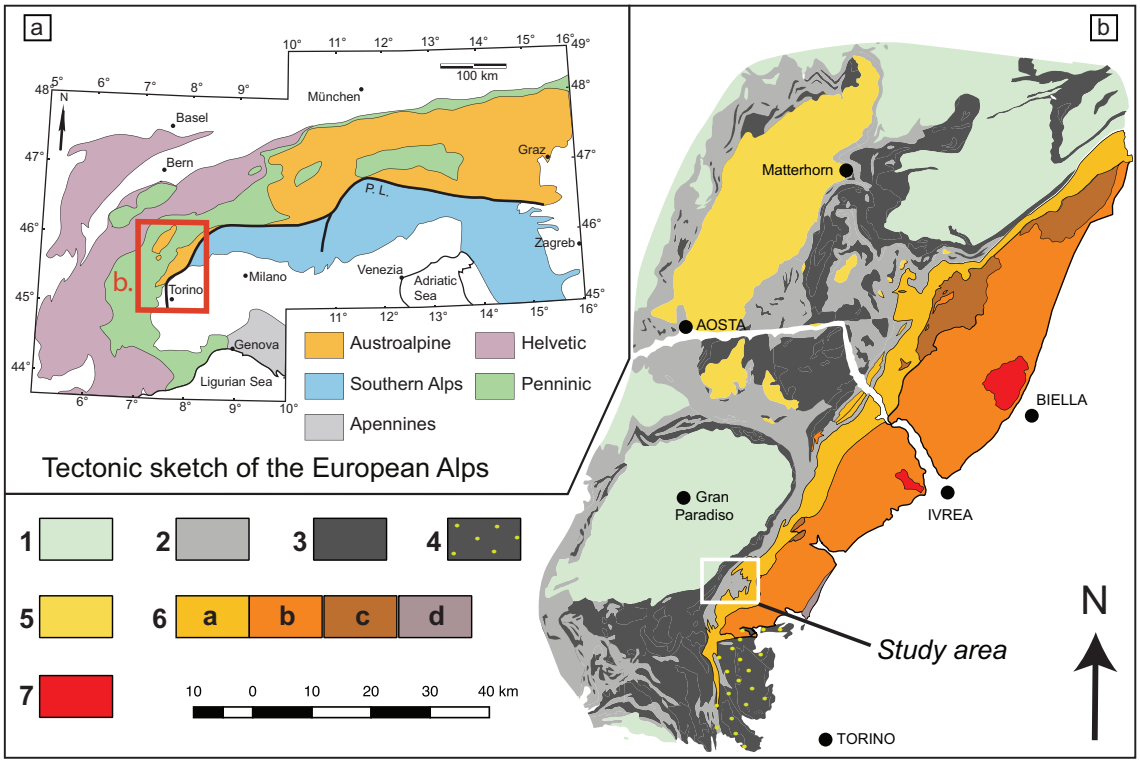

Figure 1. (**a**) Simplified tectonic scheme of the Alps with the different structural domains. The red rectangle locates the tectonic map in (**b**). P.L. = Periadriatic Lineament. (**b**) Simplified tectonic map of the Western Alps. The study area is located by the white rectangle (Figure 2). Legend: 1 = Penninic continental nappes; 2 = Piemonte Zone Mesozoic metasediments; 3 = Piemonte Zone metabasic and ultrabasic rocks; 4 = Lanzo Massif ultrabasics; 5 = Dent Blanche nappe and other Austroalpine continental klippen; 6 = Sesia-Lanzo Zone (Austroalpine Domain) - Gneiss Minuti Complex (**a**), Eclogitic Micaschists Complex (**b**), II Dioritic-Kinzigitic Zone (**c**) and Rocca Canavese Thrust Sheets (**d**); 7 = Tertiary Plutons (Biella and Traversella).

The Lago di Monastero-Punta Gias Vej area (Lanzo Valleys) offers the observation of the articulated boundary between the PZ and SLZ, a dense interlocking of ophiolitic and continental material, produced by the Alpine subduction-related structural evolution [13], in which slices of serpentinite are quite common (Figures 2 and 3a). As recently shown, in the axial portion of orogenic belts serpentinites are useful tools to unravel the oceanic and orogenic evolution of meta-ophiolite in subduction complexes e.g., [8,18–22].

Our goal is to unravel the PTdt evolution of Punta Gias Vej serpentinite from the Lanzo Valleys subduction complex, and to explore whether this evolution can be achieved during an ocean/continent subduction. For this purpose the inferred tectono-thermal peak conditions will be compared with the predictions of a 2D numerical simulation of an ocean/continent subduction system, at different time steps, in order to give clues about the time and the paleogeography of peak conditions.

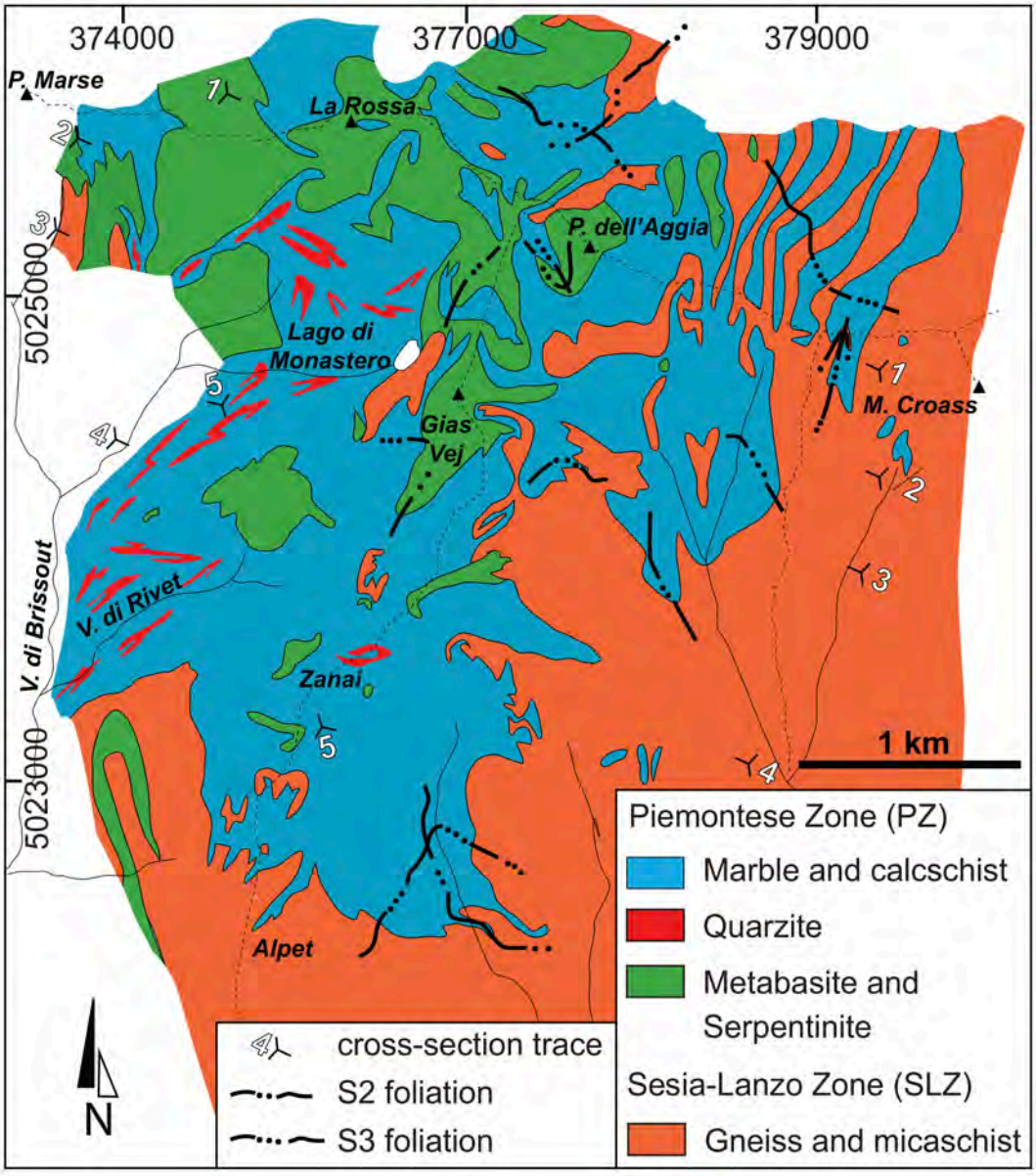

Figure 2. Interpretative geological map of Gias Vej - Lago di Monastero area modified after [13]. Coordinate system WGS 84 - UTM 32N.

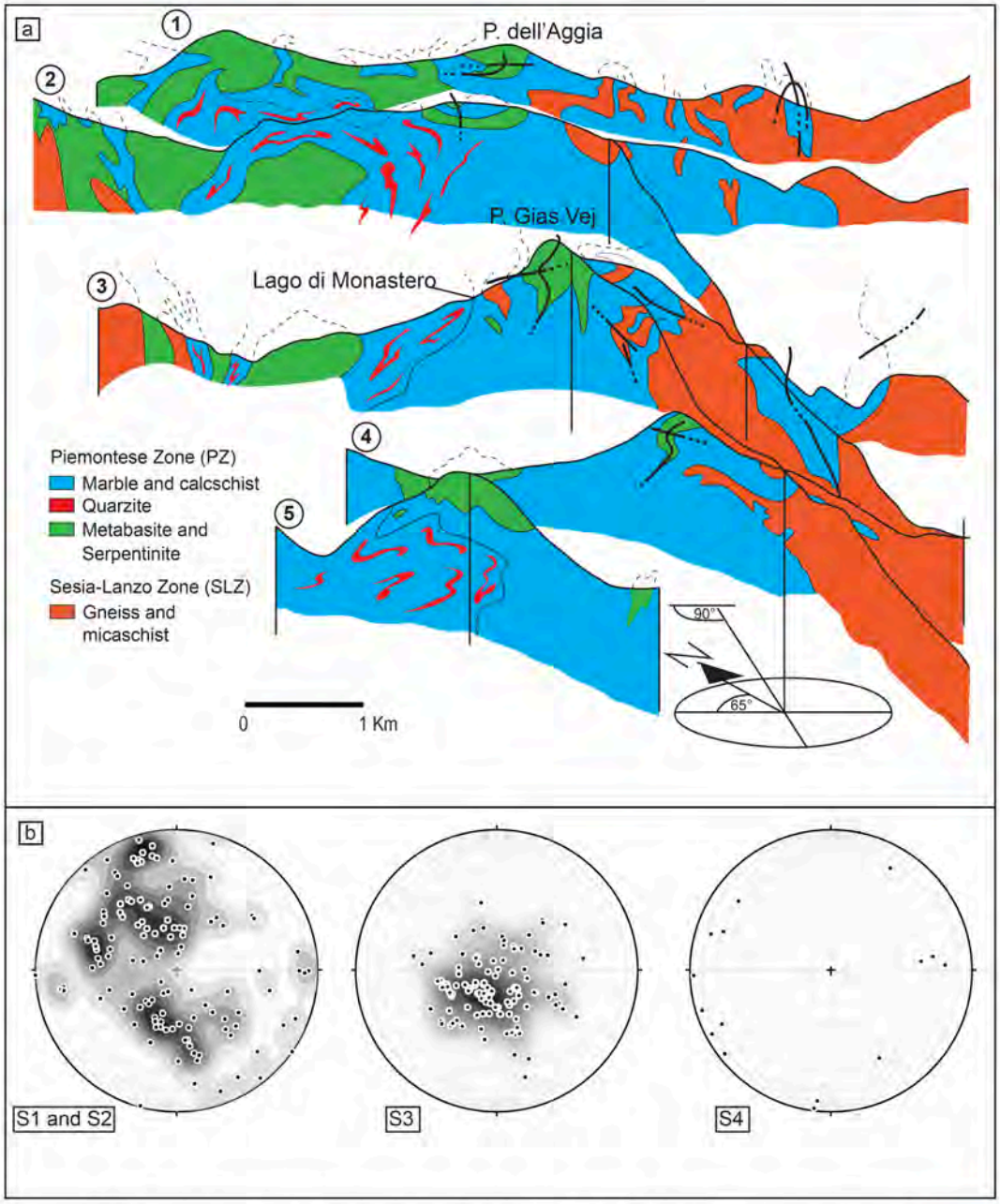

Figure 3. (**a**) Simplified cross sections (1-5) of Gias Vej - Lago di Monastero area redrawn after [13] showing the complex 3D structural pattern, due to transpositive folding and refolding during high pressure Alpine metamorphism and exhumation-related re-equilibrations, responsible for the multi-scale mingling, which originate a new cm to km-scale lithostratigraphy between continental rocks and calcschists. Axial plane trajectories of successive groups of folds are distinguished by the number of dots. Traces of the cross sections (1-5) are reported in Figure 2. (**b**) Stereographic projections (Schmidt net, lower hemisphere) of successive foliations (S1, S2, S3 and S4) of Gias Vej area (density plots and poles).

2. Geological Setting

The axial zone of the Western Alps (Figure 1a), comprised between the Periadriatic Lineament and the Penninic Front, contains units of continental and oceanic origin tectonically mixed during burial and exhumation consequent to the Alpine subduction and collision e.g., [23–31]. The investigated serpentinites are located in the Lanzo Valleys (upper part of the Tesso Valley): the main masses occur in hundreds meter-sized bodies between Punta Gias Vej and Punta dell'Aggia, where the rocks of

the ophiolitic PZ (Penninic domain) are tectonically interlocked with the continental rocks of the SLZ (Austroalpine domain), just north of the Lanzo Massif (Figures 1b, 2 and 3a).

In the PZ two different types of ophiolites have been distinguished in the Aosta Valley (northern portion of the Western Alps) on the basis of the lithological association and metamorphic assemblages, namely the Combin and Zermatt-Saas Zones, that correspond to the Upper and Lower Piemonte Zones, respectively, in the southern part of the Western Alps e.g., [5,32]. The Combin-type, or Upper Piemonte Zone, ophiolite sequence mainly comprises carbonate to terrigenous flysch-type metasediments, commonly including intercalations of metabasites and minor serpentinite slices [2,32,33]. Usually the top of the ophiolitic sequence is dominated by manganiferous quartzites and other oceanic sediments [34,35]. The dominant metamorphic imprint is recorded under greenschist-facies conditions, with mica ages at 36–40 Ma e.g., [36], although some relics of epidote-blueschist-facies minerals have been described e.g., [33,35,37,38].

The Zermatt-Saas-type, or Lower Piemonte Zone, ophiolite sequence consists of huge ultramafic and mafic bodies and minor associated metasedimentary cover; serpentinites are the most abundant rocks, often enclosing rodingite bodies [39–47]. Mafic rocks are Mg- and Fe- gabbros and metabasalts, locally preserving primary textures, such as pillow lavas [48–51], with a normal-MORB signature and recording a HP-UHP dominant metamorphic imprint see references in [5–7,32]. The metasedimentary cover comprises quartzites, marbles and calcschists [34,34,52–55]. Eclogite-facies metamorphic imprint is dominant in all the lithotypes and widely documented [51,53,56–58] and references therein, and UHP assemblages have been recognized i.e., Cignana and Valtournanche [21,54,59,60]. The ages of the protoliths are Jurassic and the HP metamorphism is generally dated between 70 and 40 Ma (see Table 1 and references therein).

Table 1. Summary of age data for peak P-T conditions of PZ ophiolites. ZSZ=Zermatt-Sass Zone, CZ=Combin zone, A=Antrona, Mv=Monviso, VM=Voltri Massif.

Unit	Locality	Rock	Mineral	Method	Age (Ma)	Event	Reference
ZSZ	Cignana	Eclogite	Garnet-Omphacite-Whole rock	Lu-Hf	48.8 ± 2.1	prograde	Lapen et al. [61]
ZSZ	Triftji	Metapelite	Garnet phengite inclusion	Rb-Sr	44.86 ± 0.49–43.6 ± 1.8	prograde	de Meyer et al. [62]
ZSZ	Triftji	Metapelite	Phengite (matrix)	Rb-Sr	40.01 ± 0.51–39.5 ± 1.1	prograde	de Meyer et al. [62]
ZSZ	Pfulwe	Eclogite	Garnet	Lu-Hf	48.9 ± 2.8	prograde	Skora et al. [63]
ZSZ	Chamois	Eclogite	Garnet	Lu-Hf	52.6 ± 1.7	prograde	Skora et al. [63]
ZSZ	Trockener Steg	Eclogite (continental)	Garnet-Whole rock	Lu-Hf	56.5 ± 2.7–58.2 ± 1.4	prograde	Weber and Bucher [58]
ZSZ	Cignana	Eclogite	Garnet	REE	70–80	prograde	Skora et al. [64]
ZSZ	Cignana	Eclogite	Garnet	Sm-Nd	52 ± 18 Ma	HP	Bowtell et al. [65]
ZSZ	Cignana	Eclogite	Zircon	U-Th-Pb	44.1 ± 0.7	UHP	Rubatto et al. [66]
ZSZ	Cignana	Metasediment	Zircon	U-Th-Pb	44.1 ± 0.7	UHP	Rubatto et al. [66]
ZSZ	Mellichen	Leucogabbro	Zircon	U-Th-Pb	48.8 ± 2.9	UHP	Rubatto et al. [66]
ZSZ	Mellichen	Leucogabbro	Zircon	U-Th-Pb	40.3 ± 9.2	UHP	Rubatto et al. [66]
ZSZ	Cignana	Eclogite	Garnet	Sm-Nd	40.6 ± 2.6	UHP	Amato et al. [67]
ZSZ	Cignana	Metasediments	Garnet phengite inclusion	Ar-Ar	43.2 ± 1.1–44.4 ± 1.5	UHP	Gouzu et al. [68]
ZSZ	St. Jacques	Eclogite	Garnet	Lu-Hf	39.2 ± 1.6	HP	Skora et al. [63]
ZSZ	Saas Fee	Eclogite	Garnet	Lu-Hf	38.1 ± 2.7–40.7 ± 1.8	HP	Skora et al. [63]
ZSZ	Pfulwe	Eclogite	Garnet-Whole rock	Lu-Hf	48.9 ± 4.8	HP	Mahlen et al. [69]
ZSZ	Saas Fee	Calcschists	Phengite	Rb-Sr	39.5 ± 0.1	HP-retrograde	Skora et al. [63]
ZSZ	Cignana	Quarzite	Phengite	Rb-Sr	40.7 ± 0.1	HP-retrograde	Skora et al. [63]
ZSZ	Cignana	Quarzite	Whole rock-Phengite	Rb-Sr	38 ± 2	retrograde	Amato et al. [67]
ZSZ	Tasch Valley	Metapelite	Whole rock-Phengite	Rb-Sr	38 ± 2	retrograde	Amato et al. [67]
ZSZ	Cignana (UU)	Metasediments	Phengite (matrix)	Ar-Ar	42–37 (plateaux age)	retrograde	Gouzu et al. [68]
ZSZ	Cignana (UU)	Metabasite	Phengite	K-Ar	38.5 ± 0.9	retrograde	Gouzu et al. [36]
ZSZ	Cignana (UU)	Metasediments	Phengite	K-Ar	40.9 ± 0.9	retrograde	Gouzu et al. [36]
ZSZ	Cignana (LU)	Eclogite	Paragonite	K-Ar	39.3–37.5	retrograde	Gouzu et al. [36]
ZSZ	Cignana (LU)	Eclogite	Phengite	K-Ar	37.1 ± 0.8	retrograde	Gouzu et al. [36]
ZSZ	Cignana (LCU)	Pelitic schist	Phengite	K-Ar	38.3–42.1	retrograde	Gouzu et al. [36]
ZSZ	Cignana (LCU)	Piemontite schist	Phengite	K-Ar	40.9 ± 0.9	retrograde	Gouzu et al. [36]
ZSZ	Cignana (LCU)	Eclogite	Paragonite	K-Ar	40.1 ± 0.9	retrograde	Gouzu et al. [36]
ZSZ	Cignana (LCU)	Mn-rich metasediment	Phengite	K-Ar	39.6 ± 0.9	retrograde	Gouzu et al. [36]
ZSZ	Valtournenche	Serpentinites	Zircon	U-Pb	65.5 ± 5.6	retrograde	Rebay et al. [6]
ZSZ	St. Jacques	Eclogite	Phengite	Rb-Sr	55–40	HP-retrograde	Reddy et al. [26]
ZSZ	Plan Maison	Calcschists	Phengite	Rb-Sr	48–46	HP	Reddy et al. [26]
ZSZ	St. Marcel	Talcschists	Garnet	Sm-Nd	49.6 ± 1.6	prograde	Dragovic et al. [70]
ZSZ	St. Marcel	Talcschists	Garnet	Sm-Nd	43.5 ± 1.3	HP	Dragovic et al. [70]
ZSZ	Lanzo Valleys	Ultrabasics	Phengite	Ar-Ar	45–30	HP-retrograde	Hunziker et al. [71]
ZSZ	various	various	Phengite	K-Ar	72–37	HP-retrograde	Delaloye and Desmons [72]
CZ	Cignana	Calcschists	Phengite	K-Ar	35.7–41.2	retrograde	Gouzu et al. [36]
CZ	Gressoney	Calcschists	Phengite	Rb-Sr	45–36	HP-retrograde	Reddy et al. [26]
CZ	Cottian Alps	Calcschists	Phengite	Ar-Ar	62–55	HP	Agard et al. [73]
CZ	Cottian Alps	Calcschists	Phengite	Ar-Ar	51–45	retrograde	Agard et al. [73]

Table 1. *Cont.*

Unit	Locality	Rock	Mineral	Method	Age (Ma)	Event	Reference
CZ	Cottian Alps	Calcschists	Phengite	K-Ar/Ar-Ar	57.6 ± 2.8	HP?	Liewig et al. [74]
CZ	Cottian Alps	Calcschists	Phengite	K-Ar/Ar-Ar	50.2 ± 2.7	HP?	Liewig et al. [74]
CZ	Cottian Alps	Radiolarites	Phengite	K-Ar	85.4 ± 3.5	HP	Bonhomme et al. [75]
CZ	Cottian Alps	Calcschists	Phengite	K-Ar	74–40	HP-retrograde	Takeshita et al. [76]
CZ	Cottian Alps	Calcschists	Phengite	K-Ar	49.5 ± 1.1	HP	Takeshita et al. [77]
CZ	Cottian Alps	Calcschists	Phengite	K-Ar	95–60	HP	Caby and Bonhomme [78]
CZ	various	Calcschists	Phengite	K-Ar	49–37	HP-retrograde	Delaloye and Desmons [72]
A	Passo del Mottone	Amphibolite	Zircon	Pb-U	38.5 ± 0.7	HP	Liati et al. [79]
A	Alpe la Balma	Eclogite	Garnet-Whole rock	Lu-Hf	42–45.5	HP	Herwartz et al. [80]
Mv	Lago Superiore	Eclogite	Garnet-Whole rock	Lu-Hf	49.2 ± 1.2	prograde-HP	Duchene et al. [81]
Mv	Lago Superiore	Metamorphic vein	Zircon	U-Pb	45 ± 1	HP	Rubatto and Hermann [82]
Mv	Lago Superiore	Eclogitic mylonite	Phengite	Rb-Sr	41.6 ± 0.4	HP	Cliff et al. [83]
Mv	Lago Superiore	Eclogitic mylonite	Garnet-Clinoyroxene	Sm-Nd	60 ± 12	HP	Cliff et al. [83]
Mv	Lago Superiore	Eclogitic metagabbros	Phengite	Ar-Ar	48–53 Ma	HP	Monié and Philippot [84]
VM	Voltri	Eclogite	Phengite	Ar-Ar	49.0 ± 0.4	HP	Federico et al. [85]
VM	Voltri	Blueschists	Phengite	Ar-Ar	43.5 ± 1.7	HP-retrograde	Federico et al. [85]
VM	Voltri	Metasediments	Muscovite	Ar-Ar	32.9 ± 0.8	retrograde	Federico et al. [85]

In the Lanzo Valleys, rocks from the PZ are mixed with those of the SLZ continental crust, and show variable lithostratigraphic settings and heterogeneous metamorphic evolutions, with climax conditions ranging from greenschist-facies in the Middle Orco Valley, where metasediments dominate [15], to eclogite-facies conditions in the Lanzo Valleys, where slices of eclogites, metagabbros, variably re-equilibrated metabasites and serpentinites are mingled with calcschists and quartzites, together with slices of SLZ gneisses [13]. The Lanzo Valleys intersect the southernmost portion of the SLZ (Figure 1b), the largest portion of continental crust from the Austroalpine domain eclogitized during the Alpine convergence e.g., [23,30,86–89]. To the West it is bounded by the PZ, to the East by the Canavese Lineament and to the South by the Lanzo Massif. The rocks of the SLZ have been exhumed to shallow crustal levels before the continental collision and the emplacement of the Biella and Traversella Tertiary plutons e.g., [28,90,91].

The SLZ is classically divided into four complexes: the II Dioritic-Kinzigitic Zone (IIDK), the Gneiss Minuti Complex (GMC), the Eclogitic Micaschists Complex (EMC) and the Rocca Canavese Thrust Sheets (RCT). The IIDK is constituted by metapelites and metabasites and preserves a pervasive pre-Alpine HT metamorphic imprint [86,92–95]. The GMC and the EMC consist of metapelites, metagranitoids, metabasites, ultramafics and impure marbles, and display a dominant Alpine metamorphic imprint that developed under greenschist-facies conditions in the GMC and under eclogite-facies conditions in the EMC. Both complexes locally preserve HT pre-Alpine mineral relics, and in the GMC, eclogitic relic assemblages of early Alpine age are sheltered in metapelites, metabasites and metagranitoids. These two complexes recorded heterogeneous Alpine metamorphic histories, among which it is discontinuously possible to recognize the record of a prograde blueschist-facies imprint, overprinted by eclogite-facies imprint, and successively re-equilibrated under blueschist- and greenschist-facies conditions. The Alpine metamorphic history developed under a low T/depth ratio (<10 °C/km), compatible with cold subductions, which persisted until the exhumation of the SLZ e.g., [13,23,86–88,94,96–109]. The RCT is characterized by pre-Alpine continental and upper mantle rocks with a climax Alpine metamorphic imprint under blueschist-facies conditions; here no relics of eclogite-facies assemblages have been described to date [101,110–115]. Mineral ages interpreted as related to the Alpine HP metamorphism vary between 90 and 65 Ma [81,91,109,116–119], whereas the greenschist-facies re-equilibration predates Biella and Traversella plutons emplacement [90,106] and therefore is older than 41–42 Ma [120].

As mentioned above the investigated serpentinites are located in the Lanzo Valleys, more precisely in the northern Tesso Valley (Punta Gias Vej) at the southern border between the SLZ and the PZ (white square in Figure 1b), not far from the triple junction between these two domains and the Lanzo Ultramafic Massif [121–124] and references therein. Here, the PZ is constituted by serpentinites with minor ophicalcites and rodingites, metabasites with relics of omphacite-bearing metagabbros and eclogites, calcschists, grey and white marbles and quartzites [13]. The SLZ comprises metagranitoids, metapelites, tholeiitic to alkaline metagabbros and metabasites that recorded eclogite-facies metamorphism [13,104,125,126].

The boundary between the PZ and the SLZ is deformed and four groups of superposed ductile structures have been detected (Figures 2 and 3a) [13]. Rootless isoclinal folds are associated with a pervasive S1 foliation (D1 structures); D2 structures are tight to isoclinal folds associated with a dominant S2 foliation. D3 comprises tight to open folds showing various styles depending on different rock rheology: tight folds and crenulation cleavage occur in calcschists whereas open folds develop in quartzites, without a new differentiated axial plane foliation. D4 gentle folds have sub-vertical axial planes, locally associated with a disjunctive cleavage.

3. Mesostructures

During field-work four groups (D1-D4; Figures 2–4) of superposed ductile structures have been recognized in both continental and oceanic affinity rocks, coherently with the structural outline of previous work [13]. D1 structures comprise up to meter size isoclinal rootless D1 folds, generally intrafolial and responsible for the strong disruption of rock layers. These folds are associated with a pervasive axial plane foliation (S1) showing very variable orientation, due to successive refolding (Figure 3b).

D2 tight to isoclinal folds with sub-vertical axial planes are associated with an axial plane foliation (S2) that is the dominant fabric at the kilometer scale, mainly dipping 50° towards NE (Figures 3b and 4b–d). S2 is a variably differentiated crenulation cleavage.

D3 folds are open, with sub-horizontal axial planes generally dipping 30° towards NW (Figures 3b and 4a–d). During D3 a pervasive axial plane foliation does not develop and when it is present, it is generally associated with chevron-like folds. D3 structures have a constant spatial orientation throughout the area and the weak local dispersions are due to the refraction induced by rock viscosity contrasts. Locally, D3 shear zones develop with mylonitic texture. D4 is testified by long-wavelength undulations, with sub-vertical axial planes, that are less pervasive than D2 and D3 folds.

Schmidt's projections show two specular bundles of data that reflect the hips of the undulations (Figure 3b). The interference patterns between the D2 and D3 folds are always of type 3 [127], while those between D3 and older folds (the latter rarely distinguishable from each other due to the local lack of direct overlapping between D2 and D1) are both of type 3 and 2. Interference patterns between D4 folds and the older ones have rarely been observed, and locally D4 fold axes show an angle of 40–60° with D2 and of 25–40° with D3 fold axes. Interference pattern of type 3 between D4 and D1 or D2 and D1 folds are locally observed. All these characters suggest a strong disruption and reorientation of the oldest folds, especially D1 ones.

D1 to D4 structures commonly affect serpentinites, metabasites enclosing metagabbro and eclogite relics, calcschists, marbles and quartzites from PZ and metapelites and metaintrusives from SLZ (Figure 4). Lithologic boundaries are re-oriented parallel to S2 and to D2 fold limbs; D2 is responsible for transposing and repeating layers of calcschists, metabasites and gneisses in a multilayer stack, consisting of decimetric to tens of meters thick levels, which marks the contact between the PZ and the SLZ.

Punta Gias Vej is mainly made of foliated and folded serpentinites, which constitute the hinge of an isoclinal D2 synform, folded by D3 folds with a slightly inclined axial plane (Figure 4d). The dominant fabric in serpentinite is S2, locally crenulated by D3 micro-folds. Metabasites within the serpentinites constitute most of the quaternary slope debris at the base of the mountain. Some metabasites occur in boudins or lenses of eclogites characterized by alternating compositional layers marking a pre-S2 foliation. Red layers are mainly constituted of red garnet, green layers of omphacite, black ones of glaucophane and dark green ones are rich in Na-Ca amphibole (Figure 4e).

Gias Vej serpentinites have generally a mylonitic texture (Figure 5a) and include olivine-, clinopyroxene- and olivine-Ti-clinohumite-clinopyroxene-rich layers (Ol-Ti-Chu-Cpx layers) or lenses, or olivine porphyroclasts wrapped by S2 mylonitic foliation. The dominant lithotype is mylonitic serpentinite (Figure 5a). Ol-Ti-Chu-Cpx layers (Figure 5b) are ten-centimeter-thick layers; their rims are crenulated by D2 but S2 is not recorded within them (Figure 5c). Serpentinite with olivine porphyroclasts is a green to yellow 20 cm-thick layer, strongly affected by S2 foliation (Figure 5d). Olivine layers (Ol layers, Figure 5e) are generally preserved as yellowish, coarse-grained, boudinaged layers wrapped by S2; Clinopyroxene layers (Cpx layers) constitute millimeter- to a few centimeters-thick anastomosed whitish domains, generally wrapped by and transposed into S2 foliation (Figure 5f). Ol-Ti-Chu-Cpx layers and serpentinite with Ol layers have mainly coronitic texture predating S2 and, therefore, they preserve pre-D2 mineral assemblages.

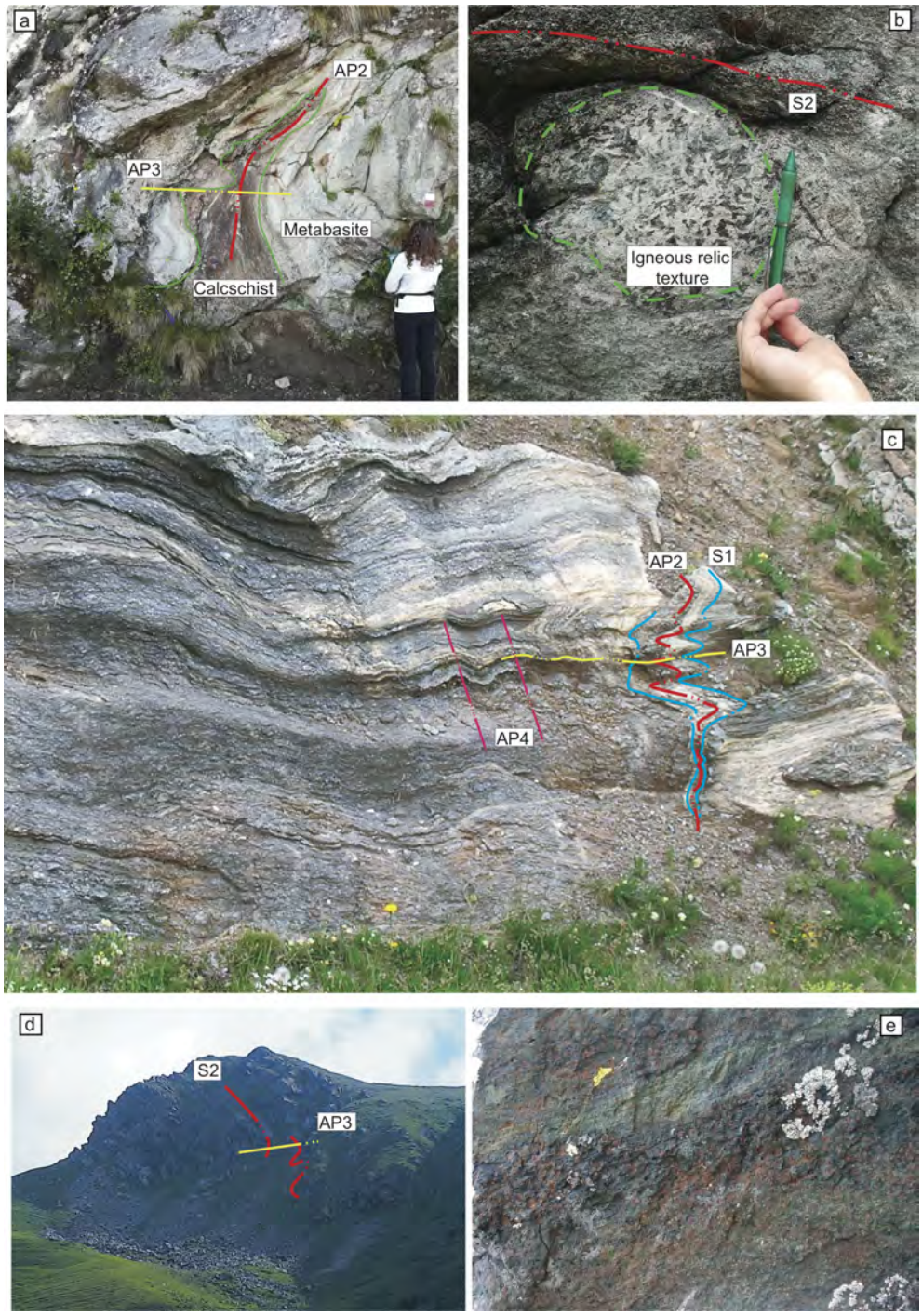

Figure 4. (**a**) Interference pattern of type 3 between D2 (isoclinal) and D3 (open) folds in metabasites and metasediments from the PZ. AP2 and AP3 indicate the traces of D2 and D3 fold axial planes, respectively. (**b**) Metabasite in which a relic volume with gabbroic texture with centimeter amphiboles is wrapped by S2. (**c**) White marble layers in calcschists of the PZ mark the overprinting relationships between S1 (light blue trace) D2 (red trace = AP2), D3 (yellow trace = AP3) and D4 (pink trace = AP4) folds. (**d**) P.ta Gias Vej is mainly constituted by serpentinites in which the dominant fabric is S2 (red trace) that is affected by D3 folding with slightly inclined axial plane (yellow trace). (**e**) Foliated eclogite relic in metabasite: alternating layers omphacite-rich (green) and garnet-amphibole-rich (dark blue with red spots) mark pre-S2 foliation. Eclogite relics generally occur in boudins, metric to hectometer in size, wrapped by S2 in metabasites. Long side of the photograph = 30 cm.

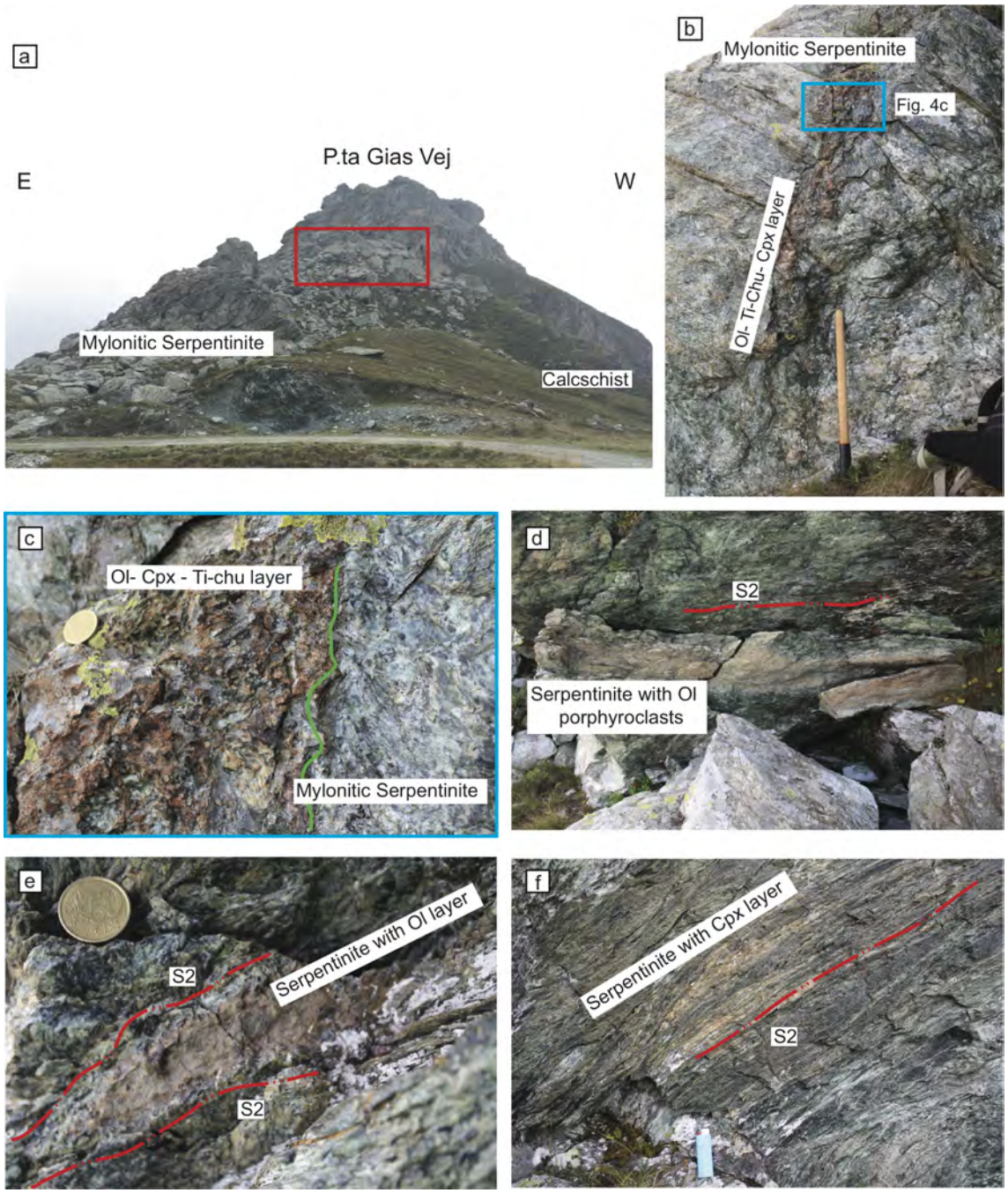

Figure 5. (**a**) Panoramic view of the north slope of Punta Gias Vej with mylonitic serpentinite overlying calcschists. The red rectangle locate the outcrops showed in b, c, d, e and f. (**b–c**) Ol-Cpx-Ti-Chu layer crenulated by D2 folds in the mylonitic serpentinite. (**d**) Serpentinite with Ol porphyroclasts layer re-oriented parallel to S2 foliation in the mylonitic serpentinite. (**e**) Serpentinite with Ol layer wrapped by S2 foliation. (**f**) Serpentinite with fine-grained Cpx layer transposed along S2.

4. Microstructures

The interesting variety of mineralogical assemblages in the Gias Vej serpentinites has been the subject of an accurate microstructural analysis aimed at identifying equilibrium parageneses during the successive deformation stages that have been identified by the mesostructural analysis, and recorded through the Alpine evolution. Samples for microstructural analysis were selected to represent most steps of the tectono-metamorphic history, to ensure an accurate reconstruction of the PTdt path. Mineral abbreviations are according to Whitney and Evans [128] and minerals are labelled according to the relative deformation stage, coherently to Table 2.

As highlighted above, the dominant foliation in the serpentinites is S2, which in the case of Gias Vej serpentinites, is generally mylonitic; the included layers have instead a predominantly coronitic fabric and are generally wrapped by S2. Their pre-D2 internal texture is sometimes complex and in some cases successive stages of textural and mineralogical re-equilibration are individuated (pre-D2a and pre-D2b) if not related to a foliated fabric, or D1 when instead there is a foliation with clear relationships with D2).

Mylonitic serpentinite is a very fine-grained rock containing Atg, minor Mag, Chl and Ilm and shows a pervasive mylonitic S2 foliation, frequently with s-c fabric (Figure 6a,b). Atg2 occurs in sub-millimeter fibers marking the dominant foliation with their SPO. Mag2 constitutes trails of porphyroblasts aligned along the S2 foliation (Figure 6a). Locally, S2 wraps small lenses of mylonitic serpentinite whose internal foliation S1 marked by Chl + Mag is at high angle with respect to S2 (Figure 6b). Millimeter aggregates of Mag1 and Mg-Chl1, with rims of Fe-Chl2, are wrapped by S2 foliation and locally preserve an internal foliation S1 that is at low angle to S2. Small pre-D2 oval domains of Atg and Mag are wrapped by S2: Mag forms globular grains, Atg constitutes radial fibers that are rimmed by tangential Atg fibers (Figure 6c). S2 is often crenulated and is either parallel or at high angle to the enclosed layers that in turn are not affected by S2. Locally crenulated Ti-Chu granoblastic veins are preserved in S2 microlithons, variably replaced by randomly oriented Atg, Chl and Mag, and at a low angle with S1. Atg-Mag-Tlc straight veins cut D2 s-c fabric, S2 films and microlithons and are therefore interpreted as post-D2 (Figure 6b).

Ol-Ti-Chu-Cpx layers are not foliated and have bimodal grain size: Atg, Mag, and Ilm form a micron- to millimeter-grained matrix, in which Ol, Cpx, and Ti-Chu constitute up to centimeter-sized crystals. Pre-D2 Ol crystals are subhedral to anhedral and rounded, with undulose extinction and they are often rimmed by radial Atg2 fibers. Ol has inclusions of Atg, Mag, and Ti-Chu (Figure 6d). Conjugated D2 veins are filled by Atg + Mag and Atg + Mag + Cal and Dol. Cpx is also found as inclusions in Ol. Pre-D2 Cpx occurs as elongated anhedral crystals, is often rimmed by radial Atg and, locally, is almost completely replaced by Amp and Cal (Figure 6e). Pre-D2 Ti-Chu crystals are up to centimeter-sized, locally with tapering lamellae. They are fractured, with Atg + Cal + Mag + Ilm fillings (Figure 6f). Often Ti-Chu is rimmed by a fine aggregate of Atg and Mag. Locally, pre-D2 Ol, Cpx, and Ti-Chu display sharp edges and they constitute polygonal aggregates only partially serpentinized (Figure 6f). BSE imaging shows that both Ol and Ti-Chu have discontinuous pre-D2 Fe-poor rims with Atg and Mag inclusions (Figure 6g). Interlocking and mesh textures define the pseudomorphosed Ol and Cpx microsites. Pre-D2 Cpx and the rock matrix are crosscut by veins filled by Atg in the matrix, Atg + Mag $\pm$ Cal $\pm$ Ilm $\pm$ Tlc in olivine and Ti-Chu. Atg fibers are parallel and perpendicular to the vein in the core and rim, respectively. In the veins, rare fibers of talc occur and Ilm rims Mag. Post-D2 veins are filled with Cal and minor Amp.

Table 2. Summary of deformation stages with and mineral associations for the studied rocks.

Rock	Deformation Events			
	pre-D2		**D2**	**post-D2**
Mylonitic serpentinite	Atg + Mag + Chl marking S1 foliation		Atg + Mag + Chl + Ilm marking S2 foliation	Atg + Mag + Tlc filling veins
Ol-Cpx-Ti-Chu layer	Ol + Ti-Chu + Cpx + Spl + Atg		Atg + Mag + Chl + Ilm + Amp + Cal + Dol coronitic or in veins	Amp + Cal filling veins
	a	b		
Serpentinite with Ol layer	Ol1 + Ti-Chu1 + Mag	Ol2 + Ti-Chu2 + Mag + Atg	Atg + Mag + Chl + Tlc marking S2 foliation	Atg + Mag + Cal filling veins
Serpentinite with Ol porphyroclasts	Atg + Ol1 + Chl1 + Cr-Mag (porphyroclasts wrapped by S2) + Cal + Mgs	Atg + Ol2 + Ti-Chu + Chl2 + Mag + Dol	Atg + Chl + Mag + Cal2 marking S2 foliation	Atg + Mag filling veins
Serpentinite with Cpx layer	Cpx porphyclasts wrapped by S1	Cpx + Chl + Atg + Mag + Amp marking S1	Atg + Mag + Chl + Ilm + Amp marking S2 foliation	Atg + Amp + Tlc filling veins

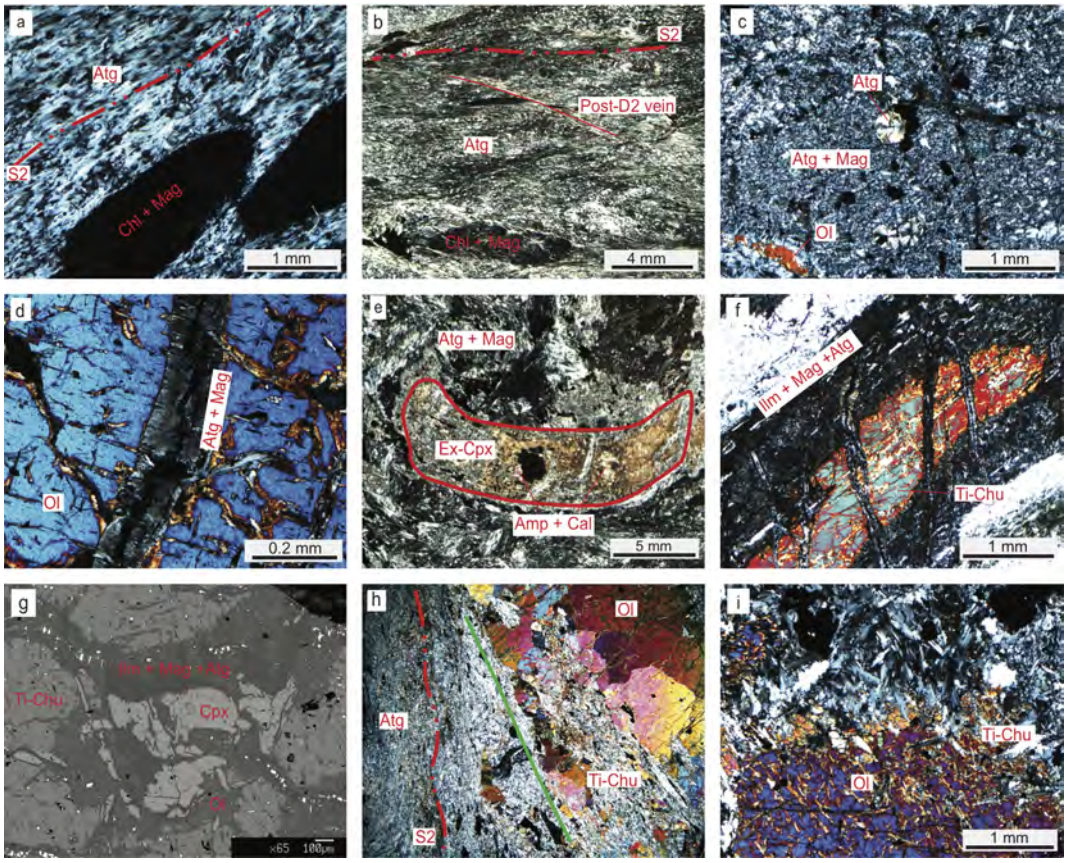

Figure 6. (**a**) Chl + Mag aggregates wrapped by S2 foliation in mylonitic serpentine marked by SPO of Atg. Crossed polars; (**b**) Panoramic view of mylonitic serpentinite with well-developed s-c fabric. Straight post-D2 veins are filled with Atg-Mag-Tlc. (**c**) Non-foliated matrix made of Atg + Mag, radial Atg superimposed on ex-Mag in a Ol-Cpx-Ti-Chu layer section. Crossed polars; (**d**) Ol porphyroclast fractured by post-D2 Atg + Mag veins. Crossed polars; (**e**) Ex-Cpx microsite replaced by Amp+Cal and surrounded by a non-foliated matrix of Atg + Mag in a Ol-Cpx-Ti-Chu layer. Crossed polars; (**f**) Ti-Chu relic rimmed by Atg + Ilm + Mag aggregate in a Ol-Cpx-Ti-Chu layer. Crossed polars; (**g**) BSE image of a Ol-Cpx-Ti-Chu layer showing Ti-Chu, Cpx and Ol aggregate with original polygonal texture. Ti-Chu is rimmed by Atg + Ilm + Mag intergrowth; (**h**) Pre-D2 Ol and Ti-Chu porphyroclasts with Atg SPO marking Pre-S2 foliation (green solid line) at low angle with S2 foliation. Crossed polars. Long side of the microphotograph = 18 mm; (**i**) Ol porphyroclast rimmed by Ti-Chu in a serpentinite with Ol layer. Crossed polars.

Serpentinite with Ol layer show S2 exclusively in serpentinite matrix, whereas the Ol layers have granoblastic fabric and the grain size is fine to coarse (3 to 20 mm). Fine-grained olivine and Ti-Chu define pre-S2 foliation at low angle with S2 in serpentinite matrix (Figure 6h) and rim coarse-grained Ol. Centimeter- to millimeter-sized pre-D2a Ol crystals with Atg1 and Mag1 inclusions are aligned in ribbons wrapped by the S2 foliation affecting the mylonitic serpentinite enclosing the layers (Figure 6h). Pre-D2a Ol has wavy extinction and is partially or fully replaced by Atg with mesh texture. Locally, rims of Fe-poor pre-D2b Ol occur around Atg1 and Mag1 in Ol1 (Figure 6d). Ti-Chu2 occurs as inclusions in Ol2 and locally rims Ol1 crystals (Figure 6i). Anhedral pre-D2a Ti-Chu crystals also occur in the isotropic Atg matrix. The boundaries between Ol-bearing layers and the mylonitic serpentinite are marked by trails of sub-millimeter Mag grains and aggregates of polygonal Ti-Chu2+Ol2 (Figure 7a). S2 in serpentinite matrix is marked by an assemblage similar to that marking S2 in mylonitic serpentinite, and post-D2 veins are filled by Atg-Mag-Cal (Table 2).

Serpentinite with Ol porphyroclasts shows pervasive S2 and has sub-millimeter to millimeter grain size. S2 is marked by the SPO of Atg and re-oriented Ol porphyroclasts, strings of Mag grains with

minor Chl, the elongation of oval Atg aggregates, and by aggregates of carbonates. Atg aggregates are wrapped by S2; they are made of Atg in mesh with minor Mag and pre-D2 Ol relicts (Figure 7b). Locally, the aggregates are rimmed by films of Mag ± Chl. Pre-D2 Ol is in ribbons parallel to the foliation (Figure 7c). Larger pre-D2 Ol crystals have undulose extinction and fractures mainly filled by Atg (Figure 7d). Ol rims are Fe-poor. Smaller pre-D2 Ol crystals form polygonal aggregates. Mag+Chl form elongated pre-D2 aggregates and locally Mag cores are Cr-rich. Locally, pre-D2b is marked by the SPO of sub-millimeter grains of Ol2 and Atg2, with sharp edges. Aggregates of Mgs with minor Atg, Mag, Cal, and Dol are found in pre-D2 lenses re-oriented parallel to S2. Dol mostly rims Cal and Mgs. Mgs constitutes a polygonal aggregate with interstitial Cal veinlets arranged into a regular net. In these Mgs-bearing aggregates Atg and Cal2 SPO are parallel to S2 (Figure 7e). Atg-Mag veins crosscut S2.

Serpentinite with Cpx layers are millimeter- to centimeter-thick and occur in the mylonitic serpentinite. The layers are made of Cpx, Atg, Chl, Amp, and minor Ox (Mag). They are folded by D2 and are either parallel or at high angle to S2 in the embedding serpentinite (Figure 7f). Cpx-bearing layers preserve an S1 foliation, mostly marked by fine-grained Cpx1, Chl1, Mag1, Atg and Amp, which wraps rare millimeter-sized pre-D1 Cpx porphyroclasts elongated parallel to S1. They are strongly deformed, as can be seen by kinked cleavages and undulose extinction (Figure 7f,g). Cpx1 grains are of sub-millimeter size, without inclusions, and they are often rimmed by Amp. SPO of sub-millimeter Atg1 fibers marks S1 foliation. Contacts between Cpx1 and Atg1 are either sharp or wriggly. Mag1 grains are parallel to S1 foliation (Figure 7h). Locally, layers are not foliated and are made by a very fine isotropic matrix of Atg, Mag, and Ilm. Post-D2 fractures are filled by Amp, Tlc, and Atg fibers perpendicular to the fractures'rim.

The deformation-metamorphism relationships are summarized in Table 2 where pre-D2, D2 and post-D2 mineral assemblages have been inferred by the above described microstructural relations in each rock type. Contrasting mineralogical assemblages have been found in different relic domains of pre-D2 fabric, and several microstructural patterns result from different overprinting combinations among D2, pre-D2 and post-D2 composite fabrics, indicating that all the analyzed ultramafic rocks underwent successive re-equilibrations during their structural evolution. They are used to derive the succession of metamorphic environments in which the Gias Vej serpentinites deformed during the Alpine convergence, and thus reconstruct their PTdt evolution.

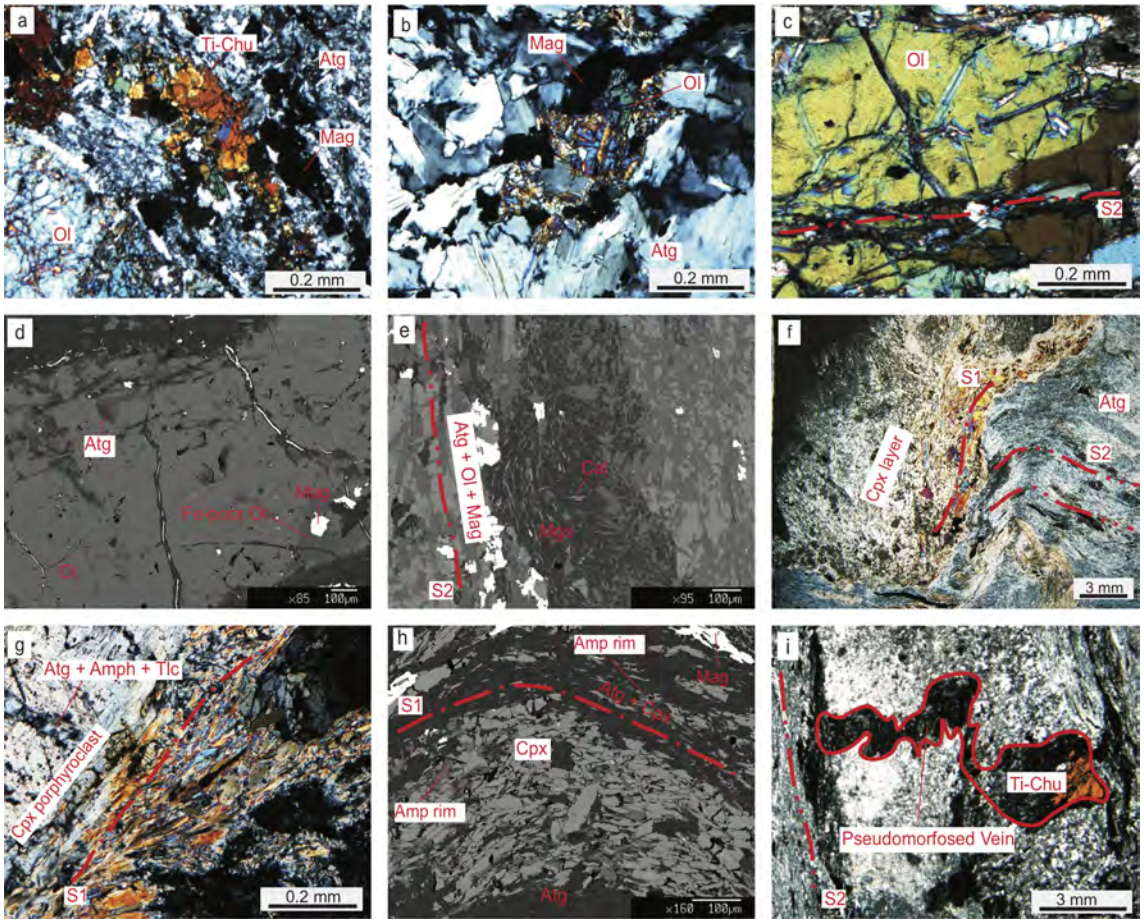

Figure 7. (**a**) Polygonal aggregate with twinned Ti-Chu and Mag between an Ol layer and the foliated (S2) matrix of Atg. Crossed polars. (**b**) Close up on Ol relic inside an ex-porphyroclast of Ol replaced by Atg and Mag, in a serpentinite with Ol porphyroclasts. Crossed polars. (**c**) Ol porphyroclast re-oriented parallel to S2 foliation with fractures filled by Atg. Crossed polars. (**d**) BSE image of a Ol porphyroclast with Fe-poor reaction-zones at the boundary with Mag and Atg. (**e**) BSE imagine of Mgs + Cal aggregates texture with Atg + Ol + Mag at the margin with Ol-rich domains that mark S2 (Serpentinite with Ol porphyroclasts). Crossed polars. (**f**) Geometric relationship between Cpx layer, S1 foliation marked by Cpx and Amp and the foliated (S2) and crenulated (D3) mylonitic matrix. S2 foliation is marked by Atg SPO, elongated Mag + Chl aggregates. Crossed Polars. (**g**) Detail of the Cpx layer with the S1 foliation marked by Cpx and Amp SPOs, Cpx porphyroclast is cut by post-D2 fractures filled with Atg + Amp + Tlc. Crossed polars. (**h**) BSE image of a layer of Cpx + Amp + Atg marking S1 foliation (serpentinite with Cpx layer). (**i**) Crenulated contact between a possibly pseudomorphosed Ti-Chu granoblastic vein replaced by randomly oriented Atg and Mag; S1 foliation, is well preserved in the microlithons of S2, marked by Atg SPO.

5. Mineral Chemistry

Minerals were analyzed with a JEOL 8200 Super Probe (WDS), at a beam current of 15 nA and 15 kV accelerating voltage operating at Dipartimento di Scienze della Terra (Milano). Natural silicates were used as standards and matrix corrections were calculated with the ZAF procedure. Mineral formulae were recalculated on the basis of the following number of oxygen atoms: 4 for Ol, 6 for Cpx, 116 for Atg [129], 28 for Chl, 4 for Mag, 3 for Ilm, and 23 for Amp. Ti-Chu formulae were recalculated on the basis of 13 cations, Fe^{3+} in ilmenite was recalculated according Droop [130], as reported in Appendix A. Olivine trace elements were obtained, from inclusion-free crystals at CNR-IGG (Pavia), with a LA-ICP-MS system coupling a 266 nm Nd:YAG laser probe with a double focusing magnetic-sector mass spectrometer, using NIST 610, NIST 611, and BCR2 standards, and GLITTER

data processing [6] and refs. therein. Spot size was 40–55 mm, laser frequency 10 Hz, acquisition was for 40–60 s preceded and followed by at least 40 s background counting (Appendix A).

Olivine is pre-D2 and has a rather homogeneous composition in all lithologies. Ol1 (pre-D2a) has Fo = 0.91–0.92, with Mg = 1.82–1.88 and Fe = 0.15–0.19. Ol2 (pre-D2b) is more Fo rich than Ol1, with Fo = 0.96–0.98, Mg = 1.92–2.0 and Fe = 0.01–0.07 (Figure 8a, Table A1). Cr varies between 1.4 and 45.1 ppm, Ca between 29.8 and 78.3 ppm and Al between 0.12 and 0.70 ppm (Table A1) in Ol1.

Ti-clinohumite has TiO_2 between 2.01 and 4.16 wt%. Almost all Ti-Chu have M/Si, where M = Mg + Fe + Mn + Ni + Ti, between 2.27 and 2.39. Pre-D2b Ti-Chu has M/Si $<$ 2.3 and lower Fe content, 0.18–0.68 apfu and Ni content, 0.07–0.20 apfu, than pre-D2a, whereas pre-D2a has M/Si $>$ 2.30, Fe = 0.21–0.8 apfu, mostly between 0.72–0.78 apfu, and Ni 0.15–0.35 apfu (Figure 8b, Table A2). Mn is consistently low, 0.03–0.06 apfu, and Ti content varies widely, though it is usually lower in pre-D2b (rims) than in pre-D2a (cores). F and Cl were not detected.

Clinopyroxene is diopside with very small compositional variations. Cpx in all lithologies is Mg rich, with X_{Mg} = 0.97–1, and may contain up to 0.15 wt% Cr_2O_3 and 0.12 wt% NiO (Table A3), especially in Cpx cores from Ol-Ti-Chu-Cpx layers, that are usually less Fe-rich (0.58–0.8) than rims (Fe = 0.68–1.43, Table A3).

Serpentine is mostly antigorite, with X_{Mg} = 0.90–0.98. Chemical variations are not associated with microstructural position (i.e., different foliations or pseudomorphs on different domains), or lithological type. Cr_2O_3 may be up to 1.49 wt% in pseudomorphoses after Ol core, NiO may be up to 0.53 wt% (Table A4).

Chlorite is mostly pennine with a few talc-chlorite analyses (Figure 8c, Table A5). Pre-D2 Chl is always Fe poor, with Fe = 0.43–0.51 apfu and Mg = 9.95–10.14 apfu. Cr content may be up to 0.41 apfu in serpentinite with Ol porphyroclasts. Chl2 is usually more Fe-rich, with Fe = 0.51–1.73 and Mg = 9.87–11.16. In serpentinite with Ol layer, chlorite is more Fe-rich (1.02–1.73 apfu) and Al-poor (0–0.16) than in all other lithologies, and is mostly talc-chlorite (Table A5).

Amphibole is tremolite, in every rock type and microstructural site. The only exception is amphibole from Ol-Ti-Chu-Cpx layers from veins and pseudomorphs after Cpx, i.e., pre-D2, which are zoned and vary from actinolite to edenite (Figure 8d). In these Amp, that can be classified as tremolite to edenite, the Na/(Na + Ca) and Al/(Al + Si) ratios are higher than in Act from other lithologies, and vary between 0.08–0.25 and 0.02–0.14 respectively (Figure 8e, Table A6). Na varies from 0.47–0.63 apfu in cores to $<$0.24 in rims, whereas it is not present in tremolite (Table A6).

Spinel is always magnetite, except for Cr-rich cores. In serpentinite with Ol porphyroclasts, spinel porphyroclasts have chromite rich cores, with chromite content up to 55%, MgO up to 11.69 wt% and Mn up to 5.21 wt% (Figure 8f, Table A7). Mn and Mg content in spinel are slightly higher in serpentinite with Ol porphyroclasts and in serpentinite with Ol layers, where the Cr-rich cores are found, than in other lithologies.

Ilmenite has been analyzed in Ol-Ti-Chu-Cpx layers and in Cpx layers. It may have Mn up to 20.06 wt% and MgO up to 9.57 wt% (Table A8). *Talc* is Mg rich, with X_{Mg} = 0.97–0.99 in serpentinite with Cpx layer. In one sample from Ol-Ti-Chu-Cpx layer it has lower X_{Mg} = 0.76–0.77 (Table A9). *Carbonates* are Cal, Mgs and Dol (Table A10), the last two occur only as relics with respect to S2.

6. Metamorphic Conditions

Metamorphic conditions have been determined using a combination of methods, to take advantage of different approaches (Figure 9a). pre-D2 temperatures have been estimated according to the Cr, Al and Ca thermometer in olivine [131], using trace elements measured by ICPMS on 10 grains of olivine (Table 3). Al and Cr thermometer in Olivine gives a temperature, expressed as mean value from the 10 analyses, of T = 556 °C at P = 2.0 GPa, and 573 °C at 2.5 GPa (T error = ±15 °C). Cr in Olivine gives a temperature, expressed as mean value from 10 analyses, of T = 582 °C at P = 2.0 GPa, and 603 °C at 2.5 GPa (T error = ±15 °C). These ranges are represented in Figure 9a by pink and blue dashed crosses, respectively.

Table 3. Olivine trace element compositions used for thermometry and temperature estimates at 2 and 2.5 GPa.

Sample	2.16	2.16	2.16	2.16	1.8	1.8	1.8	1.8	1.8	1.8
Analysis	C8 15ol	C8 16ol	C9 17ol	C9 18ol	C4 4ol	C4 5ol	C1 6ol	C4 7ol	C8 9ol	C16 18ol
Mineral	ol	ol	ol	ol	ol	ol	ol	ol	ol	ol
Al [ppm]	0.70	0.20	0.15	0.32	0.19	0.38	0.24	0.12	0.38	0.27
Cr [ppm]	16.45	33.00	20.11	35.59	9.53	34.47	30.72	6.65	45.07	1.38
Ca [ppm]	56.01	37.88	78.28	48.82	30.38	36.45	57.36	29.78	58.20	53.39
Al-Cr T@2 GPa [°C]	611	545	528	572	540	581	554	517	581	529
Al-Cr T@2.5 GPa [°C]	630	562	545	589	557	599	572	533	599	547
Cr T@2 GPa [°C]	587	614	577	623	534	622	610	510	642	503
Cr T@2.5 GPa [°C]	608	636	598	645	554	644	632	529	665	520

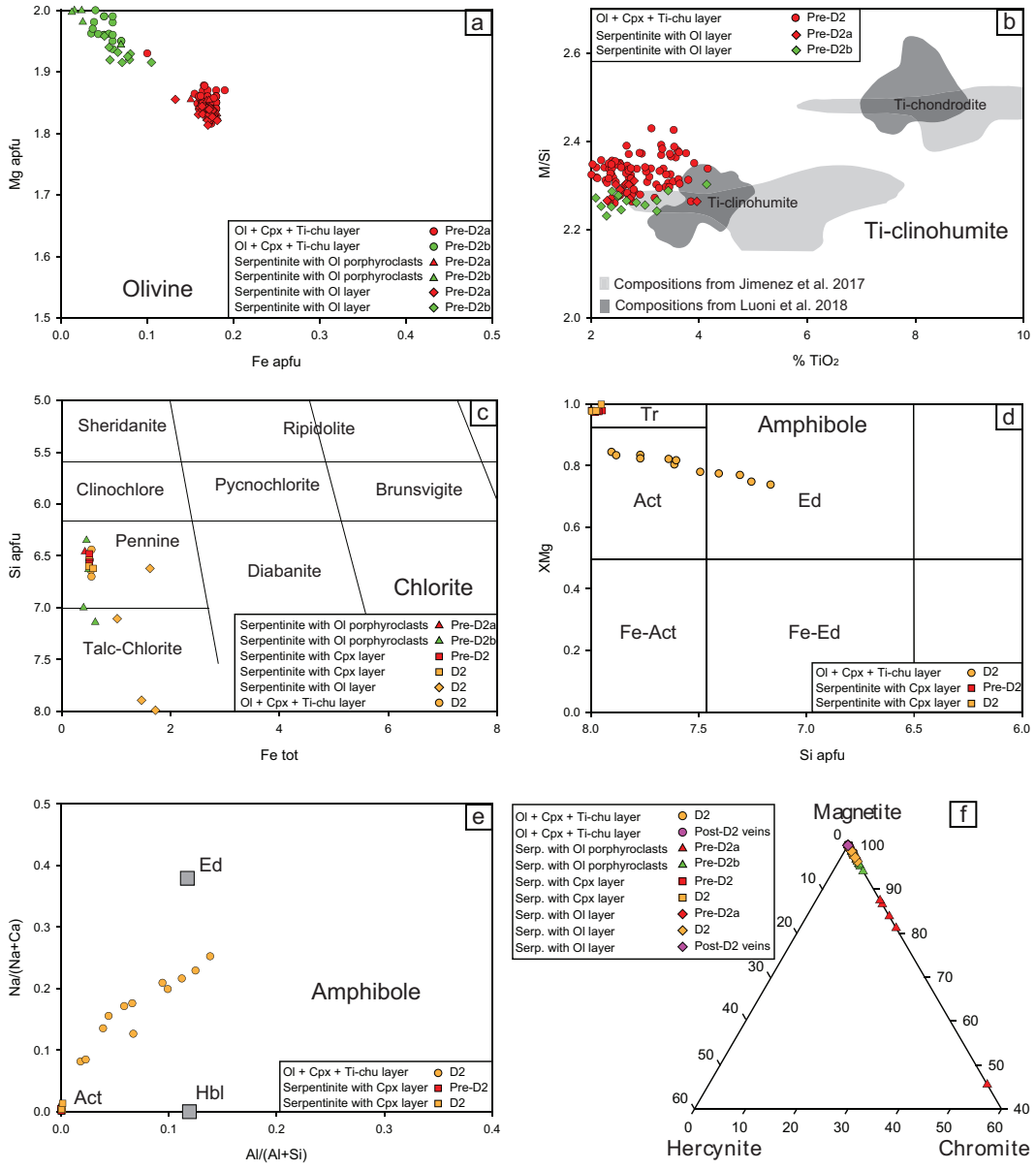

Figure 8. Mineral chemistry diagrams of the most representative minerals. (**a**) Fe vs. Mg in olivine with two clusters of data representing the first and the second generation of Ol minerals, the first one is richest in Fe; (**b**) TiO_2 wt% vs. M/Si in Ti-Clinohumite. Compositions from González-Jiménez et al. [132] - light grey - and Luoni et al. [21] - dark grey - are shown for comparison; (**c**) Chlorite classification diagram Fe_{tot} vs. Si; (**d**,**e**) Amphibole classification diagrams Si vs. X_{Mg} and Al/(Al + Si) vs. Na/(Na + Ca); (**f**) Hercynite-Chromite-Magnetite ternary diagram with spinels from different lithologies.

Average PT (AvPT) calculations have been performed on the different observed assemblages using the software THERMOCALC [133], version tc345i. The orange dashed line delimits T conditions calculated using Average T on pre-D2 assemblages of mylonitic serpentinite and serpentinite with Cpx-layer assemblages, delimiting pre-D2 temperatures in the interval 550–650 °C. The large uncertainties are due to the large PT stability field of the mineral assemblages in serpentinite, especially temperature-wise. Finally, a PT grid has been calculated using the software THERMOCALC Version tc345i, with the database ds62 [134] and end-members, in order to have an idea of the stability of mineral phases in the PT space, considering the system involving FeO, MgO, Al_2O_3, SiO_2, CaO, Fe_2O_3, H_2O, CO_2.

The main reactions of interest have been traced in Figure 9a from the full grid that was calculated considering also carbonate minerals (calcite, dolomite, magnesite, ankerite), with a fixed $aCO_2 = 0.1$. Changing the H_2O-CO_2 ratio would shift the position of some reactions, by a few to up to 30 °C. In Figure 9a, reactions have been represented using different colors to enhance readability and recognize PT fields where different assemblages are stable: black lines are reactions involving H_2O, blue ones are H_2O absent, green ones involve H_2O and CO_2 and red ones carbonates and silicates without a fluid phase. Finally, reactions involving Ti-rich humites, in light blue, are after Shen et al. [20], and have been added to represent the stability of Ti-humites that are not present in the thermodynamic database and, therefore, could not be calculated. The curves by Shen et al. [20] limit the stability field of Ti-Chu coexisting with Ol and/or Cpx (with Mgs and Dol) without Ilm (pre-D2 in Ol-Cpx-Ti-Chu layer and serpentinite with Ol porphyroclasts) above the reaction TiCh + Atg = TiCl + Ilm, and at temperatures between 520 and 620 °C, also considering the results above and the fact that Opx has never been found, while Atg is always present with Ol and/or Cpx. Hexagons represent the minerals stable in the different lithologies along a PT path, where Chiaves rocks developed pre-D2, and D2 assemblages. Atg, Mag/Spn, Chl and Amp (except for pre-D2a assemblages) are always present. All these data constrain the stability of the observed assemblages that are associated with different structures as summarized in Table 2. Summing up, pre-D2 inferred PT conditions plot at the boundary between Amphibole Eclogite- and Epidote Eclogite-facies fields [135], under a very low P/T ratio, <10 °C/km (Figure 9b). D2 conditions are more complex to determine, as the sin-D2 mineral assemblages are stable over a wide PT range. Nonetheless, the hexagons in Figure 9a represent the assemblages observed in different lithologies of Chiaves serpentinite, until the assemblage Atg + Mag + Chl + Ilm + Cal ($\pm$ Amp $\pm$ Tlc $\pm$ Dol) is stable. Calculations performed on such assemblage in different lithologies using Average P and the program THERMOCALC suggest a first rough estimate of 0.8 $\pm$ 0.3 GPa and 450 $\pm$ 50 °C, at the boundary between Blueschist- and Epidote Amphibolite-facies conditions (Figure 9b). The final exhumation is recorded by post-D2 assemblages (grouping assemblages that form coronitic replacements after D2 fabrics and minerals marking S3), with Atg, Mag, Tlc and Cal stable, at lower pressures, in the greenschist-facies conditions, coherently with mineral assemblages marking D3 fabrics in metabasites and metasediments associated with Gias Vej serpentinites (Figure 9b).

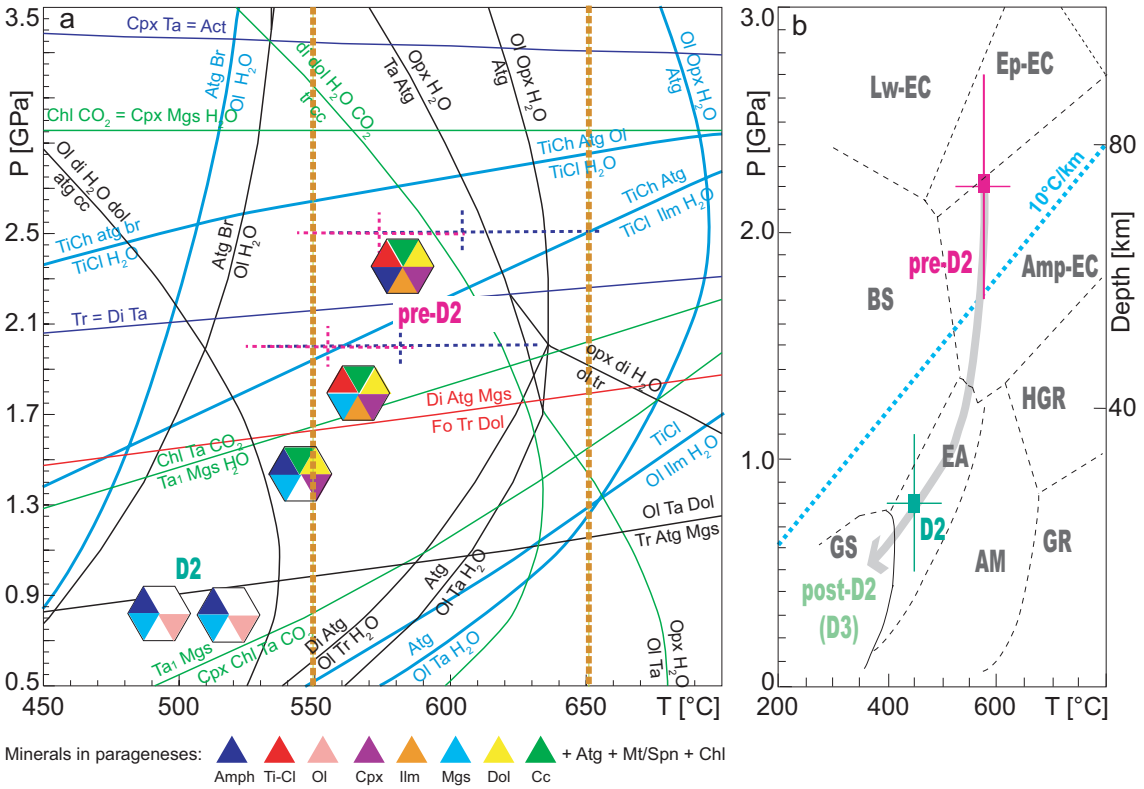

Figure 9. (**a**) PTdt path followed by Chiaves Serpentinite. PT projection is calculated using end-members and THERMOCALC software with a fluid with $aCO_2 = 0.1$. Reactions in black involve H_2O, blue ones are H_2O absent, green ones involve H_2O and CO_2 and red ones carbonates and silicates without fluid phase. Reactions involving Ti-rich humites, in light blue, are after Shen et al. [20]. Ta1 corresponds to tschermak-talc, i.e., TaTs end-member in THERMOCALC. The orange dashed line reports T conditions calculated using AvT on pre-D2 assemblages of mylonitic serpentinite and serpentinite with Cpx-layer assemblages. Pink and blue dashed crosses are the T conditions calculated using Al and Cr and Cr content of olivine, respectively [131]. Hexagons represent the minerals stable in the different lithologies along a PT path, where Chiaves rocks registered pre-D2, and D2 assemblages. Atg, Mag/Spn and Chl are always present. (**b**) Facies in PT space from Ernst and Liou [135] and PTdt path for Chiaves serpentinite (grey arrow).

7. Geodynamic Modeling and Tectonic History

The PTdt evolution of the Gias Vej serpentinites developed in a cold thermal regime ($P/T<10$ °C/km) during the subduction of the Tethys oceanic plate below the Adria plate, as generally interpreted in the literature synthesized in the geological setting. The exhumation of crust and mantle rocks during an oceanic subduction may occur within the mantle of the overriding plate, consequent to the rheological weakening induced by extensive serpentinization of the mantle wedge [8,29,115,136–140]. To understand whether the metamorphic history of Gias Vej serpentinites can be achieved within a subduction system, we use a 2D finite element method to simulate an ocean-continent subduction, and we compare the PT peak data inferred from the serpentinites with the thermal evolution generated by the modeled subduction system. The thermal states, which influenced the metamorphic evolution of Gias Vej serpentinites, can be compared with those predicted by the model to get some hints about the most likely ages for achieving the PT peak conditions of serpentinites and the tectonic setting in which the metamorphic imprint of peak conditions can develops (i.e., distance from the trench and depth).

7.1. Setup

The model setup is described by an oceanic lithosphere, representing the Alpine Tethys, and a continental lithosphere, representing the upper Adria plate. The SLZ is generally interpreted as part of the Adria plate subducted and deformed under HP conditions together with part of PZ ophiolites, in agreement with the geodynamic scenario widely proposed for the Alpine subduction system e.g., [23,25,29,141,142] and references therein. The physics of the crust-mantle system is described by coupled equations for continuity, conservation of momentum, and conservation of energy. Computations were done using the ASPECT code version 2.2.0 [143–146], which includes the shear heating. A visco-plastic rheology is assumed for the materials with dislocation creep mechanism. The plasticity limits viscous stresses through a Drucker Prager yield criterion. The model is incompressible. The material and rheological parameters used in the simulation are listed in Table 4.

Table 4. Material and rheological parameters used in the simulation. References: (1) Afonso and Ranalli [147]; (2) Schoen [148]; (3) Ranalli [149]; (4) Wilks and Carter [150]; (5) Hilairet et al. [151]; (6) Petersen and Schiffer [152]; (7) Karato and Wu [153].

Parameter	Unit	Upper Continental Crust	Lower Continental Crust	Upper Oceanic Crust	Lower Oceanic Crust	Mantle
Heat Production	Hr (mW m^{-3})	1.5	1.5	0.02	0.02	
Thermal Conductivity	K (W m^{-1} K^{-1})	2.1	2.1	1.8	2.6	4.3
Rheology		Dry granite	Dry mafic granulite	Serpentine	Gabbro	Dry olivine
Thermal diffusivity	k (m^2 s^{-1})	9.60×10^{-7}	9.60×10^{-7}	8.60×10^{-7}	8.60×10^{-7}	1.74×10^{-6}
Heat capacity	Cp (J kg^{-1} K^{-1})	750	750	750	750	1000
Density	r0 (kg m^{-3})	2900	2900	3150	3150	3400
Thermal expansivity	a (1 K^{-1})	3.00×10^{-5}	3.00×10^{-5}	3.00×10^{-5}	3.00×10^{-5}	3.00×10^{-5}
Prefactor dislocation creep	A (Pa^{-n} s^{-1})	1.13×10^{-28}	8.83×10^{-22}	1.00×10^{-21}	1.99×10^{-11}	2.41×10^{-16}
Stress exponent	n	3.2	4.2	1.0	3.4	3.5
Activation energy	Q (J mol^{-1} Pa^{-1})	1.23×10^{5}	4.45×10^{5}		4.97×10^{5}	5.40×10^{5}
Activation volume	V (m^3 mol^{-1})					1.50×10^{5}
Angle of internal friction	f					30
Cohesion	Pa	1.00×10^{8}	1.00×10^{8}	2.00×10^{7}	2.00×10^{7}	2.00×10^{7}
References		1,2,3	1,2,4	1,2,5,6	1,2,4	1,2,7

An initial continental lithospheric thickness of 100 km, including 40 km of continental crust, is assumed (Figure 10) to represent an originally thinned passive margin corresponding to the passive Adria margin [8,9,154–159]. An oceanic lithospheric thickness of 95 km with 10 km-thick crust is chosen to represent an age of ca. 40 Myr for the Tethys Ocean [8,27,29,115], based on the cooling model of a semi-infinite half-space which accounts for the effects of melt extraction, solid phase transitions, and radiative thermal conductivity [160], and characterized by a slow spreading rate (2.5 cm/yr full spreading).

The upper oceanic crust is generally strongly affected by hydrothermal alteration at mid-ocean ridges, thermal fracturing, and it is covered by oceanic sediments. Furthermore, intense serpentinization affects the oceanic mantle that can be episodically exhumed at ocean floor [7,161–165]. For this reason, the upper oceanic crust is assumed to be composed by a 5 km-thick layer of porous and fractured basalts and serpentinites. Compared to the upper oceanic crust, the lower oceanic crust is considered to be little affected by hydrothermal circulation and it is assumed formed by gabbros Table 4 [161,163–166].

To simulate plate convergence, a horizontal velocity of 3 cm/yr [29,140] is imposed along the left boundary throughout the oceanic lithosphere (Figure 10). To balance the lateral inflow an outflow is prescribed along the left boundary from the lithosphere depth to the bottom. The bottom and right boundaries are free-slip while the top boundary is treated as a free-surface (Figure 10). The model runs for 30 Myr of oceanic subduction, i.e., from 75 to 45 Ma in order to cover the entire range of ophiolite ages synthesized in Table 1.

7.2. Natural Data vs. Model Predictions

With the continuous subduction of the oceanic lithosphere below the continental lithosphere, the subduction system progressively cools down (Figure 11). The inferred PT peak conditions of Gias Vej serpentinites (pre-D2) are compared with the thermal state predicted by the numerical model of subduction zone (Figure 11). Since serpentinites from the Zermatt-Saas (or Lower Piemonte Zone)-type ophiolite sequence have been interpreted as affected by ocean floor metasomatism, therefore representing the upper part of the oceanic lithosphere, we focus on the geological setting recorded by the material that belongs to the upper oceanic crust at different timing of the tectono-metamorphic history. The metamorphic imprints of Gias Vej peak conditions occurred at pressure of 1.7–2.7 GPa and temperature of 520–620 °C (Figure 9b). No radiometric age associated with this stage are available in the literature. Therefore, we compare the inferred PT conditions with those corresponding with the different stages of the evolving subduction system. The oldest age proposed for the prograde path of Zermatt-Saas-type ophiolite is 70–80 Ma Table 1 [64]. Therefore, we selected 70 Ma as the oldest age to be compared with the PT peak conditions of Gias Vej serpentinites (Figure 11). The youngest age is controlled by the onset of the continental collision. Radiometric ages of ca. 42 Ma have been recently proposed for Traversella pluton, in the Austroalpine domain of the Western Alps, which shows a clear contamination by continental material related to the beginning of the continental subduction [120]. Therefore, we selected 45 Ma as the youngest possible climax-age for the comparison between model prediction and inferred PT conditions from natural data (Figure 11).

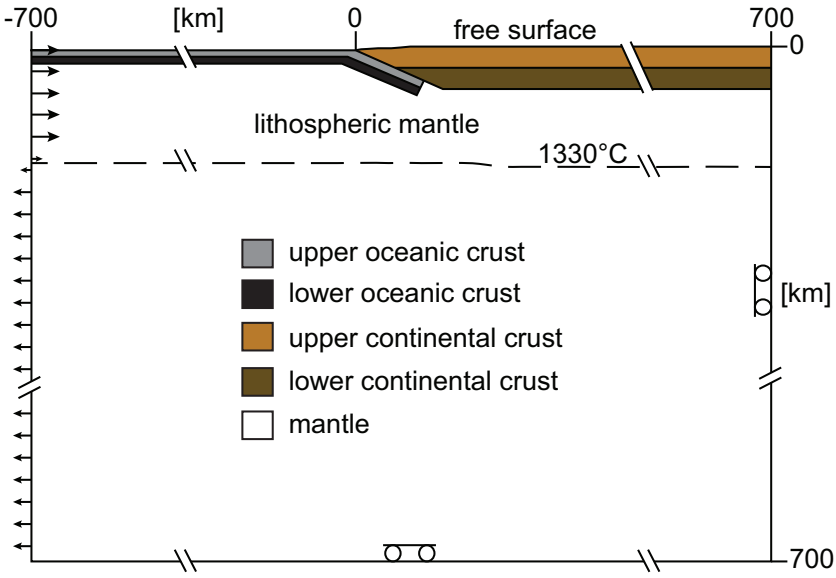

Figure 10. Model setup. The model domain is 1400 km wide and 700 km deep. The lithosphere thickness is defined by the 1330 °C isotherm. The velocity boundary conditions correspond to a free-slip condition along the bottom and the right boundaries of the domain. An inflow velocity of 3 cm/yr is fixed along the left boundary throughout the lithosphere and an outflow velocity is fixed up to the bottom to balance the flux. The upper boundary is treated as a free surface. The materials included in the model account for the upper and lower oceanic crust, upper and lower continental crust, and mantle (see Table 4 for material parameters and rheology).

All the selected stages show a fitting between the PT peak conditions of Gias Vej serpentinites and the thermal state of the oceanic crust during the subduction. However, the fitting is limited to a small portion of the upper oceanic crust at 45 Ma, while is limited to the lower oceanic crust at 70 Ma (Figure 11a,g). A good agreement is obtained for the comparison at 60 Ma, where almost the entire upper oceanic crust and part of the lower crust fit the PT conditions of Gias Vej serpentinites (Figure 11c). Even at 50 Ma most of the upper oceanic crust reaches a thermal state compatible with

that of the peak conditions of Gias Vej serpentinites (Figure 11e). On the basis of the comparison with the numerical model of subduction system, ages of 60–50 Ma are the most likely stages to achieve the PT peak conditions inferred for the Gias Vej serpentinites. The peak conditions of Gias Vej serpentinites in the subduction system are achieved at a distance of 115–145 km from the trench and at ca. 60–90 km depth considering an age of 60 Ma for the achievement of pre-D2 peak conditions (Figure 11c,d), and at a distance of 135-160 km from the trench and at ca. 70–90 km depth considering instead an age of 50 Ma (Figure 11e,f).

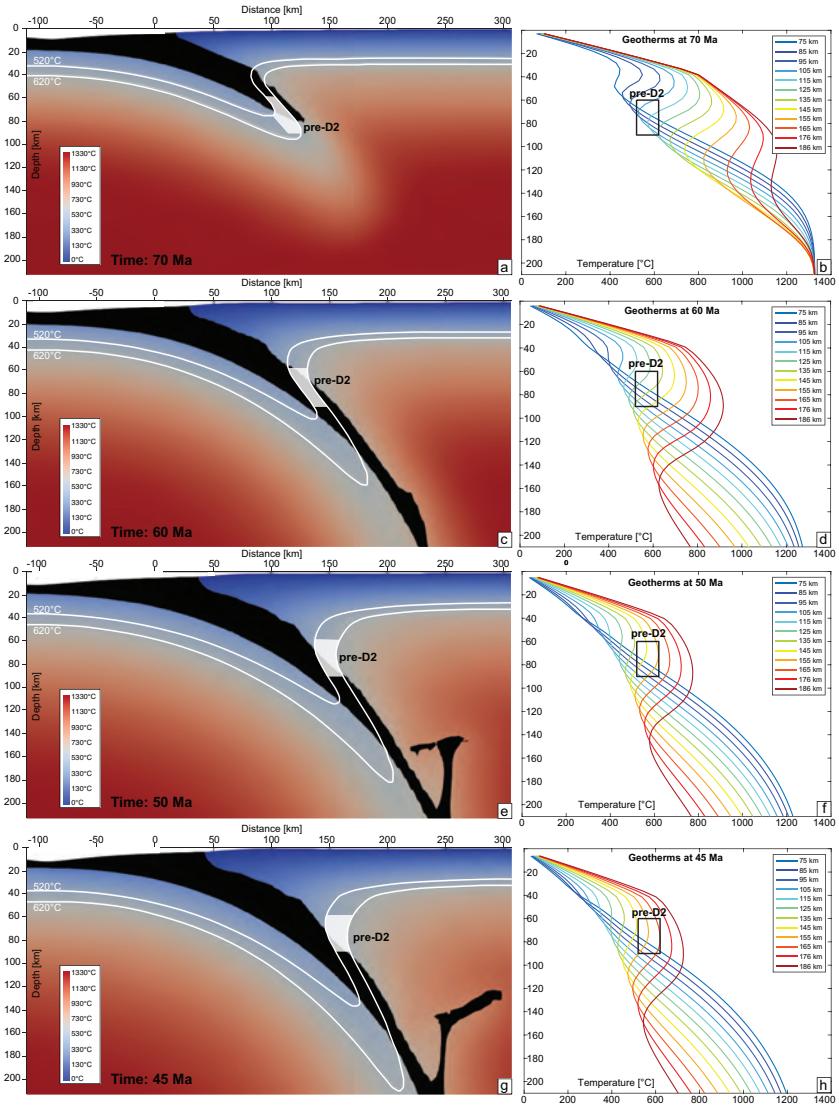

Figure 11. Results of the simulation represented by tectonic setting (**a,c,e,g**) and related geotherms extrapolated at different distances from the trench (**b,d,f,h**) at 70 Ma (**a,b**), 60 Ma (**c,d**), 50 Ma (**e,f**) and 45 Ma (**g,h**). Black color represents the oceanic crust. White isotherms represent the temperature range inferred for the peak conditions of Gias Vej serpentinites (pre-D2). The PT peak conditions are represented by white shaded areas (left) and black box (right). A good agreement is obtained for the comparison at 60 Ma (**c**), where almost the entire upper oceanic crust and part of the lower crust fit the PT conditions of Gias Vej serpentinites, and at 50 Ma (**e**), where most of the upper oceanic crust reaches a thermal state compatible with that of the peak conditions of Gias Vej serpentinites. The peak conditions in the subduction system are achieved at a distance of 115–145 km from the trench and at ca. 60–90 km depth for the stage at 60 Ma (**d**), and at a distance of 135–160 km from the trench and at ca. 70–90 km depth for the stage at 50 Ma (**f**).

8. Summary and Conclusions

The detailed structural and petrographic analysis of the serpentinites of Gias Vej allowed to identify the successive mineral assemblages constraining the PT conditions for the development of pre-D2, D2, post-D2 (D3) fabrics, thus adding a quantitative estimate of the Alpine peak conditions in a portion of the PZ still poorly explored for this aspect.

Four superposed groups of ductile structures have been individuated in Val di Lanzo serpentinites and associated metabasites and metasediments from the PZ: here D1 rootless and D2 isoclinal folds are variably refolded during D3 and D4. Relic foliated (S1) or coronitic (pre-D2) fabrics wrapped by S2 dominant foliation are marked by eclogite-facies mineral assemblages, both in metabasites-ultramafites and in metasediments. D2 and D3 fabrics are instead marked by blueschist/epidote amphibolite- and greenschist-facies parageneses, respectively (see also Table 2). PT conditions inferred from different serpentinite types indicate that pre-D2 fabrics developed at T of 570 $\pm$ 50 °C and P $>$ 1.8 GPa and D2 structures developed at T of 450 $\pm$ 50 °C and P of 0.8 $\pm$ 0.3 GPa. Post-D2 re-equilibration occurred under greenschist-facies conditions (Figure 9), in agreement with what is indicated by mineral assemblages marking D3 fabrics in the associated metasediments and metabasites. The lack of radiometric age determinations in this portion of the PZ (Table 1) makes the attribution of absolute ages to the inferred tectono-metamorphic stages aleatory.

A numerical model has been performed for exploring the physical reliability of the geodynamic context proposed for the development of climax mineral assemblages in Val di Lanzo serpentinites. The model simulates an ocean-continent subduction (2D finite element method), in agreement with the Alpine geodynamic scenario. Simulation times for oceanic subduction have been constrained by available radiometric ages, unfortunately mainly localized in the northern part of the PZ from the Western Alps (Table 1). Model predictions indicate that the inferred PT climax conditions are achieved and maintained for a long time, during an interval of ca. 30 Myr of oceanic lithosphere subduction, even though a best-fit between predicted and estimated PT conditions occurs in a time span that would fall between Paleocene and lower Eocene (50–60 Ma). According to the forecast, this age range can therefore be the one potentially favorable for the development of peak conditions.

The comparison between model results and inferred PT peak conditions allows the vertical restoration of Gias Vej serpentinites during the subduction, and suggests that the pre-D2 mineral assemblages may have developed between 60 and 90 km depth, at a distance of 115–145 km from the trench, during Paleocene, or alternatively at ca. 70–90 km depth, at a distance of 135–160 km from the trench, during lower Eocene (Figure 11). These results, suggesting a potential vertical paleogeography on the basis of the modeled thermal state between 60 and 50 Ma, indicate that the geochronological exploration of the metasediments and metabasites with HP parageneses, associated with Gias Vej serpentinites, is necessary in order to: (a) better define the geodynamic outline of the Alpine subduction also in this sector of the belt; (b) provide useful information to refine and verify the proposed geodynamic scenario.

Finally, the PTdt evolution of the serpentinites confirms that the ophiolites deformed and interdigitated with the continental Austroalpine rocks at the south end of the SLZ belong to the ZS-type, as already qualitatively deduced on the basis of peak assemblages in the surrounding metabasites and metasediments. This result highlights the heterogeneity of ophiolite types from the PZ that are tectonically implicated with the rocks of the Adriatic continental margin during the Alpine subduction, since CZ-type ophiolites are described a little further north in Valle dell'Orco [15].

The tectonic picture emerging from recent structural and petrological studies carried out along the boundary between the PZ and the southern SLZ indicates that during the Alpine convergence slices of oceanic lithosphere, recording different thermal and structural imprints during burial and exhumation paths, are tectonically sampled and mixed with rocks of Adria continental margin. Such an integration of petrological and structural analyses is the key to identifying the common paths that oceanic and continental crustal slices recorded during their involvement in the subduction system.

Author Contributions: Conceptualization, M.I.S., G.R. and M.R.; Data curation, M.A., P.L., G.R. and M.I.S.; Formal analysis, P.L., G.R., M.R. and M.I.S.; Investigation, M.A. and P.L.; Supervision, M.I.S.; Visualization, M.A., G.R., M.R. and M.I.S.; Writing original draft, M.A., P.L., G.R., M.R. and M.I.S. All authors have read and agreed to the published version of the manuscript.

Funding: This research was funded by Universitá di Milano - Linea B (PSR2019_IBOLLATI), FRG2019 Rebay, Studio Ciocca funded P.L.'s PhD scholarship.

Acknowledgments: The authors acknowledge the editors and the insightful suggestions by the three anonymous reviewers that greatly improved the text. We thank the Computational Infrastructure for Geodynamics (https://geodynamics.org) which is funded by the National Science Foundation under award EAR-0949446 and EAR-1550901 for supporting the development of ASPECT. Results here presented have been developed in the frame of the MIUR Project "Dipartimenti di Eccellenza 2017".

Conflicts of Interest: The authors declare no conflict of interest. The funders had no role in the design of the study; in the collection, analyses, or interpretation of data; in the writing of the manuscript, or in the decision to publish the results.

Appendix A. Representative EMPA Mineral Analyses for the Analyzed Rocks

Table A1. Olivines.

Rock Analysis Structure	Ol-Ti-Chu-Cpx Layer		Serpentinite with Ol Porphyroclast		Serpentinite with Ol Layer	
	CH2-8-C12-19 1	CH2-8-C13-20 2	GV3.4-C1-19 1	GV3.4-C1-18 2	GV5.8-C1-2 1	GV5.8-C1-1 2
SiO_2	41.03	41.97	40.35	41.25	41.04	41.98
TiO_2	0.02	0.02	0.01	0.00	0.00	0.03
Al_2O_3	0.00	0.01	0.00	0.02	0.01	0.00
Cr_2O_3	0.00	0.00	0.08	0.00	0.00	0.03
FeO	8.16	1.77	7.81	0.64	7.85	2.82
MnO	0.40	0.48	0.27	0.26	0.40	0.51
MgO	50.82	55.56	50.34	56.79	50.58	54.96
CaO	0.00	0.00	0.03	0.00	0.04	0.01
Na_2O	0.00	0.00	0.00	0.01	0.00	0.00
K_2O	0.01	0.01	0.00	0.00	0.02	0.01
NiO	0.20	0.17	0.28	0.04	0.39	0.19
Sum	100.66	100.00	99.17	99.00	100.32	100.55
Cations based on 4 oxygens						
Si	0.994	0.994	0.991	0.982	0.996	0.994
Ti	0.000	0.000	0.000	0.000	0.000	0.001
Al	0.000	0.000	0.000	0.001	0.000	0.000
Cr	0.000	0.000	0.002	0.000	0.000	0.001
Fe	0.165	0.035	0.160	0.013	0.159	0.056
Mn	0.008	0.010	0.006	0.005	0.008	0.010
Mg	1.835	1.962	1.843	2.016	1.831	1.940
Ca	0.000	0.000	0.001	0.000	0.001	0.000
Na	0.000	0.000	0.000	0.000	0.000	0.000
K	0.000	0.000	0.000	0.000	0.000	0.000
Ni	0.004	0.003	0.006	0.001	0.008	0.004
Sum	3.006	3.005	3.008	3.018	3.004	3.005
X_{Mg}	0.92	0.98	0.92	0.99	0.92	0.97

Table A2. Ti-Clinohumites.

Rock Analysis Structure	Ol - Ti-chu - Cpx Layer		Serpentinite with Ol Layer			
	CH2_16-C2-4 1	CH2-16-C3-7 2	GV5.8-C2-24 1	GV5.8-C3-28 2	GV5.8-C3-27 1	GV5.8-C5-40 2
SiO2	37.23	37.40	36.99	37.70	36.95	36.61
TiO2	4.16	3.45	2.56	2.29	2.38	2.46
Al2O3	0.00	0.02	0.00	0.01	0.00	0.01
Cr2O3	0.01	0.02	0.00	0.01	0.03	0.00
FeO	3.71	2.65	5.79	2.88	8.10	8.01
MnO	0.46	0.42	0.57	0.63	0.40	0.39
MgO	53.82	54.03	50.75	53.14	50.17	50.41
CaO	0.01	0.00	0.00	0.03	0.01	0.01
Na2O	0.01	0.00	0.00	0.02	0.00	0.01
K2O	0.01	0.00	0.01	0.00	0.01	0.00
NiO	0.19	0.17	0.15	0.18	0.27	0.25
Sum	99.61	98.16	96.83	96.88	98.32	98.17
On the basis of 13 cations						
Si	3.894	3.944	4.006	4.023	3.973	3.937
Ti	0.327	0.274	0.209	0.184	0.192	0.199
Al	0.000	0.002	0.000	0.001	0.000	0.001
Cr	0.000	0.001	0.000	0.001	0.003	0.000
Fe	0.324	0.234	0.524	0.257	0.728	0.720
Mn	0.041	0.038	0.052	0.057	0.036	0.035
Mg	8.392	8.493	8.194	8.455	8.042	8.081
Ca	0.001	0.000	0.000	0.003	0.001	0.002
Na	0.002	0.000	0.000	0.004	0.000	0.003
K	0.001	0.000	0.002	0.000	0.001	0.000
Ni	0.016	0.014	0.013	0.015	0.024	0.022
Sum	13.000	13.000	13.000	13.000	13.000	13.000
M/Si	2.34	2.30	2.25	2.23	2.27	2.30

Table A3. Pyroxenes.

Rock Analysis Structure	Ol-Ti-Chu-Cpx Layer			Serpentinite with Cpx Layer		
	CH2-1-C4-35 1	CH2-16-C11-51 2	CH2-9-C13-18 1	GV2.2-C4-50 2	GV2.2-C4-53 1	GV2.2-C4-54 2
SiO_2	56.06	55.69	55.22	55.64	55.73	54.94
TiO_2	0.02	0.01	0.03	0.00	0.00	0.05
Al_2O_3	0.00	0.01	0.00	0.00	0.04	0.00
Cr_2O_3	0.00	0.03	0.01	0.02	0.00	0.05
FeO	0.75	0.87	0.77	0.69	0.58	1.37
MnO	0.03	0.01	0.14	0.02	0.04	0.05
MgO	18.01	18.05	18.08	17.94	18.07	17.49
CaO	26.47	26.21	25.69	26.92	27.11	26.90
Na_2O	0.02	0.00	0.02	0.03	0.00	0.01
K_2O	0.00	0.00	0.00	0.01	0.00	0.00
NiO	0.00	0.06	0.08	0.06	0.01	0.01
Sum	101.37	100.94	100.04	101.32	101.59	100.87
Cations based on 6 oxygens						
Si	2.000	1.998	1.997	1.988	1.985	1.978
Ti	0.000	0.000	0.001	0.000	0.000	0.001
Al_{IV}	0.000	0.001	0.000	0.000	0.002	0.000
Al_{VI}	0.000	0.000	0.001	0.000	0.000	0.000
Cr	0.000	0.001	0.000	0.000	0.000	0.002
Fe^{3+}	0.000	0.002	0.005	0.021	0.017	0.041
Fe^{2+}	0.023	0.024	0.018	0.000	0.000	0.000
Mn	0.000	0.000	0.000	0.000	0.000	0.000
Mg	0.962	0.965	0.975	0.955	0.959	0.938
Ca	1.010	1.007	0.996	1.031	1.035	1.038
Na	0.000	0.000	0.000	0.002	0.000	1.038
K	0.000	0.000	0.001	0.002	0.000	0.001
Ni	0.000	0.002	0.000	0.001	0.000	0.000
Sum	4.000	4.000	4.000	4.000	4.000	4.000
FeO	0.750	0.790	0.610	0.000	0.000	0.000
Fe_2O_3	0.000	0.092	0.180	0.766	0.645	1.522
Ac%	0.14	0.00	0.13	0.25	0.02	0.09
Ca.FeTs%	0.00	0.17	0.24	1.05	0.86	2.14
Ca.TiTs%	0.05	0.03	0.07	0.00	0.00	0.12
Woll%	50.66	50.28	49.59	50.91	51.12	50.69
En%	47.97	48.33	48.82	47.77	47.84	46.87
Fs%	1.18	1.20	1.13	0.02	0.07	0.08

Table A4. Serpentines.

Rock Analysis Structure	Ol - Ti-chu - Cpx Layer			Serentinite with Ol Porphyroclast		Serpentinite with Cpx Layer		Serpentinite with Ol Layer			
	CH2_1-C3-16 2	CH2_8-C8-55 2	CH2_8-C11-93 1	GV3.4-C3-51 in ol	GV3.4-C1-22 2	GV2.2-C4-49 2	GV2.2-C6-66 1	GV5.8-C8-76 1	GV5.8-C1-10 2	GV5.8-C9-82 2	GV5.8-C1-5 2
SiO_2	43.87	43.98	40.30	41.55	44.07	42.77	43.70	43.44	42.97	42.76	44.32
TiO_2	0.04	0.22	0.11	0.05	0.00	0.01	0.03	0.05	0.00	0.02	0.00
$Al_2 O_3$	1.31	0.02	1.55	2.29	1.08	1.43	0.84	0.27	0.77	1.09	0.08
$Cr_2 O_3$	0.27	0.04	0.01	1.47	0.16	0.34	0.06	0.01	0.01	0.31	0.00
FeO	2.50	1.97	5.78	2.62	1.68	2.90	3.03	1.02	1.57	1.30	0.59
MnO	0.03	0.08	0.05	0.04	0.04	0.13	0.07	0.06	0.04	0.05	0.07
MgO	38.31	41.13	40.24	38.27	38.60	38.95	38.00	40.08	39.65	39.90	39.82
CaO	0.00	0.03	0.03	0.01	0.00	0.01	0.02	0.01	0.02	0.00	0.01
$Na_2 O$	0.00	0.00	0.02	0.01	0.02	0.02	0.02	0.00	0.00	0.00	0.01
K2O	0.00	0.00	0.01	0.01	0.01	0.01	0.03	0.00	0.00	0.01	0.02
NiO	0.15	0.21	0.23	0.19	0.09	0.18	0.31	0.00	0.07	0.16	0.08
Sum	86.48	87.67	88.32	86.50	85.75	86.74	86.11	84.94	85.10	85.60	84.99
Cations based on 116 oxygens											
Si	1.999	1.980	1.851	1.911	2.014	1.956	2.007	2.002	1.983	1.964	2.033
Ti	0.001	0.007	0.004	0.002	0.000	0.000	0.001	0.002	0.000	0.001	0.000
Al	0.070	0.001	0.084	0.124	0.058	0.077	0.046	0.014	0.042	0.059	0.004
Cr	0.010	0.001	0.000	0.053	0.006	0.012	0.002	0.000	0.000	0.011	0.000
Fe	0.095	0.074	0.222	0.101	0.064	0.111	0.116	0.039	0.061	0.050	0.022
Mn	0.001	0.003	0.002	0.001	0.002	0.005	0.003	0.002	0.001	0.002	0.003
Mg	2.601	2.760	2.754	2.623	2.629	2.654	2.602	2.752	2.728	2.731	2.722
Ca	0.000	0.001	0.001	0.000	0.000	0.000	0.001	0.000	0.003	0.006	0.003
Na	0.000	0.000	0.002	0.001	0.002	0.002	0.002	0.000	0.001	0.000	0.000
K	0.000	0.000	0.000	0.001	0.001	0.000	0.001	0.000	0.000	0.000	0.001
Ni	0.006	0.008	0.009	0.007	0.003	0.007	0.011	0.000	0.000	0.001	0.001
Sum	4.784	4.835	4.928	4.823	4.779	4.824	4.793	4.813	4.819	4.824	4.790
X_{Mg}	0.96	0.97	0.93	0.96	0.98	0.96	0.96	0.99	0.98	0.98	0.99

Table A5. Chlorites.

Rock Analysis Structure	Ol-Ti-Chu-Cpx Layer			Serpentinite with Ol Porphyroclast			Serpentinite with Cpx Layer	
	CH2-1-C2-9 2	CH2-1-C2-10 2	CH2-1-C10-63 2	GV3.4-C2-43 1	GV3.4-C1-1 2	GV3.4-C2-44 2	GV2.2-C5-64 1	GV2.2-C4-55 2
SiO_2	34.33	33.73	35.42	33.78	36.92	33.46	33.87	34.47
TiO_2	0.00	0.03	0.06	0.00	0.00	0.00	0.05	0.00
Al_2O_3	12.02	12.63	10.31	12.19	7.12	11.88	12.66	12.09
Cr_2O_3	1.11	0.99	1.09	1.59	2.66	3.23	1.03	0.53
FeO	3.29	3.46	3.45	2.71	2.56	2.92	3.17	3.63
MnO	0.02	0.00	0.04	0.03	0.04	0.03	0.05	0.05
MgO	35.44	35.27	36.61	35.53	37.51	35.68	34.95	34.61
CaO	0.01	0.04	0.01	0.01	0.01	0.01	0.06	0.07
Na_2O	0.00	0.00	0.02	0.00	0.00	0.03	0.02	0.06
K_2O	0.01	0.02	0.02	0.00	0.00	0.01	0.01	0.03
NiO	0.10	0.19	0.14	0.07	0.03	0.15	0.10	0.12
Sum	86.33	86.36	87.17	85.92	86.85	87.40	85.96	85.66
Cations based on 28 oxygens								
Si	6.543	6.439	6.697	6.465	6.999	6.349	6.479	6.617
Ti	0.000	0.004	0.009	0.000	0.000	0.000	0.007	0.000
Al	2.701	2.842	2.298	2.750	1.591	2.657	2.855	2.736
Cr	0.167	0.149	0.163	0.241	0.399	0.485	0.156	0.080
Fe	0.524	0.552	0.546	0.434	0.406	0.463	0.507	0.583
Mn	0.003	0.000	0.006	0.005	0.006	0.005	0.008	0.008
Mg	10.066	10.034	10.316	10.133	10.598	10.090	9.964	9.902
Ca	0.002	0.008	0.002	0.002	0.002	0.002	0.012	0.014
Na	0.000	0.000	0.007	0.000	0.000	0.011	0.007	0.022
K	0.002	0.005	0.005	0.000	0.000	0.002	0.002	0.007
Ni	0.015	0.029	0.021	0.011	0.005	0.023	0.015	0.019
Sum	20.024	20.063	20.070	20.040	20.006	20.087	20.013	19.989
X_{Mg}	0.95	0.95	0.95	0.96	0.96	0.96	0.95	0.94

Table A6. Amphiboles.

Rock Analysis Structure	Ol-Ti-Chu-Cpx Layer			Serpentinite with Cpx Layer		
	CH2-1-C5-45 2	CH2-1-C5-48 2	CH2-16-C16-90 2	GV2.2-C4-51 2	GV2.2-C4-58 2	GV2.2-C4-61 post-2
SiO_2	49.58	55.34	52.40	58.88	58.67	59.08
TiO_2	0.06	0.01	0.05	0.04	0.04	0.05
Al_2O_3	6.76	1.91	4.62	0.00	0.04	0.01
Cr_2O_3	0.44	0.25	0.36	0.05	0.02	0.01
FeO	10.07	7.44	8.67	0.89	0.91	0.99
MnO	0.04	0.09	0.08	0.12	0.18	0.13
MgO	15.80	19.17	17.01	23.81	23.86	24.03
CaO	12.15	12.29	11.95	14.06	13.58	13.91
Na_2O	2.27	1.07	1.75	0.03	0.02	0.00
K_2O	0.18	0.09	0.10	0.01	0.01	0.02
NiO	0.04	0.07	0.12	0.04	0.06	0.05
Sum	97.46	98.09	97.64	97.92	97.37	98.27
Species	edenite	actinolite	actinolite	tremolite	tremolite	tremolite
Cations based on 23 oxygens						
Si	7.166	7.770	7.492	7.997	8.004	7.994
Ti	0.007	0.000	0.007	0.004	0.004	0.002
Al_{IV}	0.834	0.230	0.508	0.000	0.000	0.001
Al_{VI}	0.317	0.086	0.271	0.000	0.006	0.001
Cr	0.050	0.028	0.041	0.005	0.002	0.001
Fe^{3+}	2.199	1.935	2.102	0.000	0.000	0.000
Fe^{2+}	1.207	0.804	1.024	0.101	0.103	0.112
Mn	0.004	0.010	0.010	0.013	0.020	0.015
Mg	3.404	4.012	3.626	4.821	4.853	4.847
Ca	1.882	1.849	1.831	2.046	1.988	2.017
Na_B	0.113	0.131	0.166	0.003	0.005	0.000
Na_A	0.523	0.159	0.319	0.008	0.003	0.003
K	0.034	0.016	0.019	0.002	0.003	0.003
Ni	0.005	0.008	0.014	0.005	0.006	0.005
Sum	17.745	17.038	17.430	15.005	14.997	15.001
Al/Al + Si	0.14	0.04	0.09	0.00	0.00	0.00
Na/Na + Ca	0.25	0.14	0.21	0.01	0.00	0.00
X_{Mg}	0.74	0.83	0.78	0.98	0.98	0.98

Table A7. Spinels.

Rock Analysis Structure	Serpentinite with Ol Porphyroclast			Ol-Ti-Chu-Cpx Layer		Serpentinite with Cpx Layer			Serpentinite with Ol Layer		
	GV3.4-C1-5 1	GV3.4-C2-39 1	GV3.4-C1-14 2	CH2-8-C16-136 1	CH2-8-C6-43 2	GV2.2-C1-9 1	GV2.2-C3-41 2	GV2.2-C2-21 2	GV5.8-C7-67 1	GV5.8-C5-46 2	GV5.8-C6-60 2
SiO_2	0.04	0.00	0.00	0.00	0.01	0.05	0.04	0.05	0.08	0.00	0.04
TiO_2	0.14	0.29	0.08	0.05	0.00	0.04	0.00	0.04	0.14	0.08	0.16
Al_2O_3	0.01	0.16	0.02	0.04	0.00	0.03	0.01	0.00	0.00	0.00	0.01
Cr_2O_3	13.67	39.58	2.98	0.04	0.04	1.17	0.04	0.11	0.11	1.56	2.55
FeO	67.91	39.34	82.42	93.99	95.34	92.72	92.86	92.41	87.77	88.53	87.21
MnO	2.40	5.21	0.86	0.25	0.11	0.07	0.08	0.08	0.88	0.82	1.13
MgO	10.87	11.69	7.50	0.57	0.18	0.09	0.06	0.08	4.97	3.55	4.16
CaO	0.01	0.00	0.00	0.00	0.00	0.02	0.07	0.19	0.03	0.01	0.00
Na_2O	0.03	0.10	0.00	0.03	0.06	0.00	0.04	0.00	0.01	0.04	0.06
K_2O	0.00	0.00	0.02	0.00	0.00	0.00	0.01	0.00	0.00	0.00	0.00
NiO	0.50	0.24	0.73	1.88	1.01	0.14	0.67	0.81	0.62	0.78	0.57
Sum	95.58	96.61	94.60	96.85	96.75	94.33	93.88	93.76	94.61	95.37	95.88
Cations based on 4 oxygens											
Si	0.001	0.000	0.000	0.000	0.000	0.002	0.002	0.002	0.003	0.000	0.001
Ti	0.004	0.008	0.002	0.001	0.000	0.001	0.000	0.001	0.004	0.002	0.004
Al	0.000	0.007	0.001	0.002	0.000	0.001	0.000	0.000	0.000	0.000	0.000
Cr	0.375	1.081	0.084	0.001	0.001	0.035	0.001	0.003	0.003	0.045	0.073
Fe^{3+}	1.617	0.904	1.912	1.996	2.002	1.957	1.999	1.991	1.984	1.953	1.919
Fe^{2+}	0.354	0.233	0.553	0.902	0.948	0.991	0.965	0.963	0.689	0.754	0.722
Mn	0.071	0.152	0.026	0.008	0.003	0.002	0.003	0.003	0.027	0.025	0.035
Mg	0.562	0.602	0.400	0.031	0.010	0.005	0.003	0.005	0.270	0.194	0.225
Ca	0.000	0.000	0.000	0.000	0.000	0.001	0.003	0.008	0.001	0.000	0.000
Na	0.002	0.007	0.000	0.002	0.004	0.000	0.003	0.000	0.001	0.003	0.004
K	0.000	0.000	0.001	0.000	0.000	0.000	0.000	0.000	0.000	0.000	0.000
Ni	0.014	0.007	0.021	0.056	0.030	0.004	0.021	0.025	0.018	0.023	0.017
Sum	3.000	3.001	3.000	2.999	2.998	2.999	3.000	3.001	3.000	2.999	3.000
Chromite	18.83	54.46	4.21	0.05	0.05	1.76	0.05	0.15	0.15	2.25	3.66
Magnetite	81.17	45.54	95.79	99.95	99.95	98.24	99.95	99.85	99.85	97.75	96.34

Table A8. Ilmenites.

Rock	**Ol-Ti-Chu-Cpx Layer**		**Serpentinite. with Cpx Layer**
Analysis	**8**	**16**	**GV2.2**
Structure	**2**	**2**	**2**
SiO_2	0.8	0.32	0.06
TiO_2	50.61	55.15	51.85
Al_2O_3	0.06	0.01	0.00
Cr_2O_3	0.03	0.00	0.02
FeO	26.23	23.57	32.21
MnO	16.58	8.88	13.54
MgO	1.85	9.57	0.4
CaO	0.01	0.15	0.01
Na_2O	0.03	0.03	0.01
K_2O	0.00	0.01	0.00
Sum	99.36	101.6	98.81
Cations based on 3 oxygens			
Si	0.020	0.007	0.002
Ti	0.950	0.959	0.992
Al	0.002	0.000	0.000
Cr	0.001	0.000	0.000
Fe^{3+}	0.059	0.068	0.014
Fe^{2+}	0.547	0.456	0.685
Mn	0.350	0.174	0.292
Mg	0.069	0.330	0.015
Ca	0.000	0.004	0.000
Na	0.001	0.001	0.000
K	0.000	0.000	0.000
Sum	2.000	2.000	2.000

Table A9. Talc.

Rock	**Ol-Ti-Chu-Cpx Layer**	**Serpentinite with Cpx Layer**	
Analysis	**16**	**GV2.2**	**GV2.2**
Structure	**post-2**	**post-2**	**post-2**
SiO_2	57.02	62.6	62.36
TiO_2	0.02	0.00	0.00
Al_2O_3	0.02	0.38	0.33
Cr_2O_3	0.00	0.00	0.06
FeO	12.26	1.00	0.72
MnO	0.18	0.01	0.01
MgO	20.95	30.34	30.32
CaO	1.10	0.02	0.06
Na_2O	0.08	0.02	0.01
K_2O	0.16	0.14	0.18
Sum	91.79	94.51	94.05
Cations based on 11 oxygens			
Si	3.970	4.002	4.003
Ti	0.001	0.000	0.000
Al	0.002	0.029	0.025
Cr	0.000	0.000	0.003
Fe^{3+}	0.075	0.000	0.000
Fe^{2+}	0.679	0.053	0.039
Mn	0.012	0.001	0.001
Mg	2.155	2.891	2.901
Ca	0.083	0.001	0.004
Na	0.009	0.002	0.001
K	0.017	0.011	0.015
Sum	7.003	6.991	6.991

Table A10. Carbonates.

Rock	Ol-Ti-Chu-Cpx Layer		Serpentinite with Ol Porphyroclast		
Analysis	16	16	GV3.4-C2-2	GV3.4-C2-2	GV3.4-C2-2
Structure	2	2	1	1	2
SiO_2	0.19	0.08	0.06	0.00	0.04
TiO_2	0.07	0.04	0.03	0.01	0.04
Al_2O_3	0.01	0.01	0.00	0.03	0.01
Cr_2O_3	0.02	0.00	0.03	0.00	0.00
FeO	0.47	0.26	0.04	0.24	0.02
MnO	0.54	0.22	0.00	0.38	0.00
MgO	22.75	0.18	18.57	47.89	0.05
CaO	30.96	60.72	45.08	0.61	65.19
Na_2O	0.00	0.03	0.06	0.00	0.00
K_2O	0.00	0.00	0.00	0.01	0.01
Sum	55.01	61.54	63.87	49.17	65.36
Cations based on 3 oxygens					
Si	0.006	0.002	0.002	0.000	0.001
Ti	0.002	0.001	0.001	0.000	0.001
Al	0.000	0.000	0.000	0.001	0.000
Cr	0.000	0.000	0.001	0.000	0.000
Fe^{3+}	0.000	0.000	0.000	0.000	0.000
Fe^{2+}	0.012	0.007	0.001	0.006	0.000
Mn	0.013	0.006	0.000	0.009	0.000
Mg	0.994	0.008	0.726	1.966	0.002
Ca	0.973	1.974	1.267	0.018	1.995
Na	0.000	0.002	0.003	0.000	0.000
K	0.000	0.000	0.000	0.000	0.000
Sum	2.000	2.000	2.000	2.000	2.000

References

1. Dal Piaz, G. Filoni rodingitici e zone di reazione a bassa temperatura al contatto tettonico tra serpentine e rocce incassanti nelle Alpi occidentali italiane. *Rendiconti della Società Italiana di Mineralogia e Petrologia* **1969**, *27*, 437–477.
2. Dal Piaz, G.; Venturelli, G.; Spadea, P.; Di Battistini, G. Geochemicl features of metabasalts and metagabbros from the Piemonte ophiolite nappe, Italian Western Alps. *Neues Jahrbuch fur Mineralogie, Abhandlungen* **1981**, *142*, 248–269.
3. Beccaluva, L.; Dal Piaz, G.; Macciotta, G. Transitional to normal MORB affinities in ophiolitic metabasites from the Zermatt-Saas, Combin and Antrona units, Western Alps: Implications for the paleogeographic evolution of the western Tethyan basin. *Geologie en Mijnbouw* **1984**, *63*, 165–177.
4. Pfeifer, H.R.; Colombi, A.; Ganguin, J. Zermatt-Saas and Antrona Zone: A petrographic and geochemical comparison of poliphase metamorphic ophiolites of the West-Central Alps. *Schweizerische Mineralogische und Petrographische Mitteilungen* **1989**, *69*, 217–236.
5. Martin, S.; Tartarotti, P.; Dal Piaz Giorgio, V. The Mesozoic ophiolites of the Alps: A review. *OGS/Bollettino di Geofisica Teorica e Applicata* **1994**, *36*, 175–220.
6. Rebay, G.; Zanoni, D.; Langone, A.; Luoni, P.; Tiepolo, M.; Spalla, M.I. Dating of ultramafic rocks from the Western Alps ophiolites discloses Late Cretaceous subduction ages in the Zermatt-Saas Zone. *Geol. Mag.* **2018**, *155*, 298–315. [CrossRef]
7. Balestro, G.; Festa, A.; Dilek, Y. Structural architecture of the Western Alpine Ophiolites, and the Jurassic seafloor spreading tectonics of the Alpine Tethys. *J. Geol. Soc.* **2019**, *176*, 913–930. [CrossRef]
8. Luoni, P.; Rebay, G.; Roda, M.; Zanoni, D.; Spalla, M.I. Tectono-metamorphic evolution of UHP Zermatt-Saas serpentinites: A tool for vertical palaeogeographic restoration. *Int. Geol. Rev.* **2020**, 1–26. [CrossRef]
9. Manatschal, G. New models for evolution of magma-poor rifted margins based on a review of data and concepts from West Iberia and the Alps. *Int. J. Earth Sci.* **2004**, *93*, 432–466. [CrossRef]
10. Picazo, S.; Müntener, O.; Manatschal, G.; Bauville, A.; Karner, G.; Johnson, C. Mapping the nature of mantle domains in Western and Central Europe based on clinopyroxene and spinel chemistry: Evidence for mantle modification during an extensional cycle. *Lithos* **2016**, *266*, 233–263. [CrossRef]
11. McCarthy, A.; Tugend, J.; Mohn, G.; Candioti, L.; Chelle-Michou, C.; Arculus, R.; Schmalholz, S.M.; Müntener, O. A case of Ampferer-type subduction and consequences for the Alps and the Pyrenees. *Am. J. Sci.* **2020**, *320*, 313–372. [CrossRef]
12. Dilek, Y.; Furnes, H. Ophiolite genesis and global tectonics: Geochemical and tectonic fingerprinting of ancient oceanic lithosphere. *Geol. Soc. Am. Bull.* **2011**, *123*, 387–411. [CrossRef]

13. Spalla, M.I.; De Maria, L.; Gosso, G.; Miletto, M.; Pognante, U. Deformazione e metamorfismo della Zona Sesia – Lanzo meridionale al contatto con la falda piemontese e con il massiccio di Lanzo, Alpi occidentali. *Memorie della Società Geologica Italiana* **1983**, *26*, 499–514.
14. Battiston, P.; Benciolini, L.; Dal Piaz, G.; De Vecchi, G.; Marchi, G.; Martin, S.; Polino, R.; Tartarotti, P. Geologia di una traversa dal Gran Paradiso alla zona Sesia-Lanzo in alta Val Soana, Piemonte. *Memorie della Società Geologica Italiana* **1984**, *29*, 209–232.
15. Gasco, I.; Gattiglio, M.; Borghi, A. Structural evolution of different tectonic units across the Austroalpine–Penninic boundary in the middle Orco Valley (Western Italian Alps). *J. Struct. Geol.* **2009**, *31*, 301–314. [CrossRef]
16. Gosso, G.; Rebay, G.; Roda, M.; Spalla, M.I.; Tarallo, M.; Zanoni, D.; Zucali, M. Taking advantage of petrostructural heterogeneities in subduction- collisional orogens, and effect on the scale of analysis. *Periodico di Mineralogia* **2015**, *84*, 779–825. [CrossRef]
17. Benciolini, L.; Martin, S.; Tartarotti, P. Il metamorfismo eclogitico nel basamento del Gran Paradiso ed in Unità Piemontesi della Valle di Campiglia. *Memorie della Società Geologica Italiana* **1984**, *29*, 127–151.
18. Debret, B.; Nicolet, C.; Andreani, M.; Schwartz, S.; Godard, M. Three steps of serpentinization in an eclogitized oceanic serpentinization front (Lanzo Massif - Western Alps). *J. Metamorph. Geol.* **2013**, *31*, 165–186. [CrossRef]
19. Jabaloy-Sánchez, A.; Gómez-Pugnaire, M.T.; Padrón-Navarta, J.A.; López Sánchez-Vizcaíno, V.; Garrido, C.J. Subduction- and exhumation-related structures preserved in metaserpentinites and associated metasediments from the Nevado–Filábride Complex (Betic Cordillera, SE Spain). *Tectonophysics* **2015**, *644–645*, 40–57. [CrossRef]
20. Shen, T.; Hermann, J.; Zhang, L.; Lü, Z.; Padrón-Navarta, J.A.; Xia, B.; Bader, T. UHP Metamorphism Documented in Ti-chondrodite- and Ti-clinohumite-bearing Serpentinized Ultramafic Rocks from Chinese Southwestern Tianshan. *J. Petrol.* **2015**, *56*, 1425–1458. [CrossRef]
21. Luoni, P.; Rebay, G.; Spalla, M.I.; Zanoni, D. UHP Ti-chondrodite in the Zermatt-Saas serpentinite: Constraints on a new tectonic scenario. *Am. Mineral.* **2018**, *103*, 1002–1005. [CrossRef]
22. Gilio, M.; Scambelluri, M.; Agostini, S.; Godard, M.; Peters, D.; Pettke, T. Petrology and Geochemistry of Serpentinites Associated with the Ultra-High Pressure Lago di Cignana Unit (Italian Western Alps). *J. Petrol.* **2019**, *60*, 1229–1262. [CrossRef]
23. Dal Piaz, G.; Hunziker, J.C.; Martinotti, G. La Zona Sesia - Lanzo e l'evoluzione tettonico-metamorfica delle Alpi Nordoccidentali interne. *Memorie della Società Geologica Italiana* **1972**, *11*, 433–460.
24. Caron, J.M.; Polino, R.; Pognante, U.; Lombardo, B.; Lardeaux, L.M.; Lagabrielle, Y.; Gosso, G.; Allenbach, B. Ou sont les sutures majeures dans les Alpes internes? (transversale Brian{ç}on-Torino). *Memorie della Società Geologica Italiana Geologica Italiana* **1984**, *29*, 71–78.
25. Polino, R.; Dal Piaz, G.; Gosso, G. Tectonic erosion at the Adria margin and accretionary processes for the Cretaceous orogeny of the Alps. *Mémoires de la Societé Géologique de France* **1990**, *156*, 345–367.
26. Reddy, S.M.; Wheeler, J.; Cliff, R. The geometry and timing of orogenic extension: an example from the Western Italian Alps. *J. Metamorph. Geol.* **1999**, *17*, 573–589. [CrossRef]
27. Handy, M.R.; Schmid, S.M.; Bousquet, R.; Kissling, E.; Bernoulli, D. Reconciling plate-tectonic reconstructions of Alpine Tethys with the geological–geophysical record of spreading and subduction in the Alps. *Earth-Sci. Rev.* **2010**, *102*, 121–158. [CrossRef]
28. Spalla, M.I.; Gosso, G.; Marotta, A.M.; Zucali, M.; Salvi, F. Analysis of natural tectonic systems coupled with numerical modelling of the polycyclic continental lithosphere of the Alps. *Int. Geol. Rev.* **2010**, *52*, 1268–1302. [CrossRef]
29. Roda, M.; Spalla, M.I.; Marotta, A.M. Integration of natural data within a numerical model of ablative subduction: a possible interpretation for the Alpine dynamics of the Austroalpine crust. *J. Metamorph. Geol.* **2012**, *30*, 973–996. [CrossRef]
30. Lardeaux, J.M. Deciphering orogeny: a metamorphic perspective. Examples from European Alpine and Variscan belts: Part I: Alpine metamorphism in the western Alps. A review. *Bulletin de la Societe Geologique de France* **2014**, *185*, 93–114. [CrossRef]
31. van Hinsbergen, D.J.; Torsvik, T.H.; Schmid, S.M.; Maţenco, L.C.; Maffione, M.; Vissers, R.L.; Gürer, D.; Spakman, W. Orogenic architecture of the Mediterranean region and kinematic reconstruction of its tectonic evolution since the Triassic. *Gondwana Res.* **2020**, *81*, 79–229. [CrossRef]

32. Gasco, I.; Gattiglio, M.; Borghi, A. Review of metamorphic and kinematic data from Internal Crystalline Massifs (Western Alps): PTt paths and exhumation history. *J. Geodyn.* **2013**, *63*, 1–19. [CrossRef]
33. Dal Piaz, G. Revised setting of the Piedmont zone in the northern Aosta valley, Western Alps. *Ofioliti* **1988**, *13*, 157–162.
34. Dal Piaz, G.; Di Battistini, G.; Kienast, J.; Venturelli, G. Manganiferous quartzitic schists of the Piemonte ophiolite nappe in the Valsesia-Valtournanche area (Italian Western Alps). *Memorie di Scienze Geologiche* **1979**, *32*, 1–24.
35. Vannay, J.; Allemann, R. La zone Piémontaise dans le Haut-Valtournanche (Val d'Aoste, ltalie). *Eclogae Geologicae Helvetiae* **1990**, *83*, 21–39.
36. Gouzu, C.; Yagi, K.; Thanh, N.X.; Itaya, T.; Compagnoni, R. White mica K-Ar geochronology of HP-UHP units in the Lago di Cignana area, western Alps, Italy: Tectonic implications for exhumation. *Lithos* **2016**, *248-251*, 109–118. [CrossRef]
37. Kienast, J.R. Le métamorphisme de haute pressionet basse température (Eclogites et Schistes Bleus): Données nouvelles sur la pétrologie de la croûte océanique Subductée et des sédiments Associés. Ph.D Thesis, Université de Paris VI, Paris, France, 1983.
38. Martin, S.; Cortiana, G. Influence of the whole-rock composition on crystallisation of sodic amphiboles (Piemonte nappe, Western Alps). *Ofioliti* **2001**, *26*, 445–456.
39. Rahn, M.; Bucher, K. Titanian clinohumite formation in the Zermatt-Saas ophiolites, Central Alps. *Mineral. Petrol.* **1998**, *64*, 1–13. [CrossRef]
40. Li, X.P.; Rahn, M.; Bucher, K. Metamorphic Processes in Rodingites of the Zermatt-Saas Ophiolites. *Int. Geol. Rev.* **2004**, *46*, 28–51. [CrossRef]
41. Groppo, C.; Compagnoni, R. Metamorphic veins from the serpentinites of the Piemonte Zone, western Alps, Italy: A review. *Periodico di Mineralogia* **2007**, *76*, 127–153. [CrossRef]
42. Fontana, E.; Panseri, M.; Tartarotti, P. Oceanic relict textures in the Mount Avic Serpentinites, Western Alps. *Ofioliti* **2008**, *33*, 105–118. [CrossRef]
43. Fontana, E.; Tartarotti, P.; Panseri, M.; Buscemi, S. Geological map of the Mount Avic massif (Western Alps Ophiolites). *J. Maps* **2015**, *11*, 126–135. [CrossRef]
44. Rebay, G.; Spalla, M.I.; Zanoni, D. Interaction of deformation and metamorphism during subduction and exhumation of hydrated oceanic mantle: Insights from the Western Alps. *J. Metamorph. Geol.* **2012**, *30*, 687–702. [CrossRef]
45. Zanoni, D.; Rebay, G.; Bernardoni, J.; Spalla, M.I. Using multiscale structural analysis to infer high-/ultrahigh-pressure assemblages in subducted rodingites of the Zermatt-Saas Zone at Valtournanche, Italy. *J. Virtual Explorer* **2012**, *41*. [CrossRef]
46. Zanoni, D.; Rebay, G.; Spalla, M.I. Ocean floor and subduction record in the Zermatt-Saas rodingites, Valtournanche, Western Alps. *J. Metamorph. Geol.* **2016**, *34*, 941–961. [CrossRef]
47. Diella, V.; Bocchio, R.; Marinoni, N.; Caucia, F.; Spalla, M.I.; Adamo, I.; Langone, A.; Mancini, L. Garnets from Val d'Ala Rodingites, Piedmont, Italy: An Investigation of Their Gemological, Spectroscopic and Crystal Chemical Properties. *Minerals* **2019**, *9*, 728. [CrossRef]
48. Bearth, P. Die ophiolite der Zone von Zermatt-Sass Fee. *Beitrag Geologische Karte Schweitz* **1967**, *132*, 1–130.
49. Dal Piaz, G.; Ernst, W. Areal geology and petrology of eclogites and associated metabasites of the Piemonte ophiolite nappe, Breuil—St. Jacques area, Italian Western Alps. *Tectonophysics* **1978**, *51*, 99–126. [CrossRef]
50. Bucher, K.; Fazis, Y.; de Capitani, C.; Grapes, R. Blueschists, eclogites, and decompression assemblages of the Zermatt-Saas ophiolite: High-pressure metamorphism of subducted Tethys lithosphere. *Am. Mineral.* **2005**, *90*, 821–835. [CrossRef]
51. Bucher, K.; Grapes, R. The eclogite-facies Allalin gabbro of the Zermatt-Saas ophiolite, Western alps: A record of subduction zone hydration. *J. Petrol.* **2009**, *50*, 1405–1442. [CrossRef]
52. Bearth, P.; Schwander, H. The post-Triassic sediments of the ophiolite zone Zermatt-Saas Fee and the associated manganese mineralizations. *Eclogae Geologicae Helvetiae* **1981**, *74*, 189–205.
53. Barnicoat, A.; Fry, N. High -pressure metamorphism of the Zermatt-Sass ophiolite, Switzerland. *J. Geol. Soc.* **1986**, *143*, 607–618. [CrossRef]
54. Reinecke, T. Very high pressure metamorphism and uplift of coesite-bearing metasediments from the Zermatt-Saas Zone, Western Alps. *Eu. J. Mineral.* **1991**, *3*, 7–17. [CrossRef]

55. Dal Piaz, G.; Bistacchi, A.; Gianotti, F.; Monopoli, B. *Note illustrative della Carta Geologica d'Italia alla scala 1:50.000 – foglio 070 Monte Cervino*; ISPRA: Roma, Italy 2015; p. 413.
56. Angiboust, S.; Agard, P.; Jolivet, L.; Beyssac, O. The Zermatt-Saas ophiolite: The largest (60-km wide) and deepest (c. 70-80km) continuous slice of oceanic lithosphere detached from a subduction zone? *Terra Nova* **2009**, *21*, 171–180. [CrossRef]
57. Groppo, C.; Beltrando, M.; Compagnoni, R. The P-T path of the ultra-high pressure Lago Di Cignana and adjoining high-pressure meta-ophiolitic units: Insights into the evolution of the subducting Tethyan slab. *J. Metamorph. Geol.* **2009**, *27*, 207–231. [CrossRef]
58. Weber, S.; Bucher, K. An eclogite-bearing continental tectonic slice in the Zermatt–Saas high-pressure ophiolites at Trockener Steg (Zermatt, Swiss Western Alps). *Lithos* **2015**, *232*, 336–359. [CrossRef]
59. Frezzotti, M.L.; Selverstone, J.; Sharp, Z.D.; Compagnoni, R. Carbonate dissolution during subduction revealed by diamond-bearing rocks from the Alps. *Nat. Geosci.* **2011**, *4*, 703–706. [CrossRef]
60. Luoni, P.; Zanoni, D.; Rebay, G.; Spalla, M.I. Deformation history of Ultra High-Pressure ophiolitic serpentinites in the Zermatt-Saas Zone, Créton, Upper Valtournanche (Aosta Valley, Western Alps). *Ofioliti* **2019**, *44*, 111–123. [CrossRef]
61. Lapen, T.J.; Johnson, C.M.; Baumgartner, L.P.; Mahlen, N.J.; Beard, B.L.; Amato, J.M. Burial rates during prograde metamorphism of an ultra-high-pressure terrane: an example from Lago di Cignana, western Alps, Italy. *Earth Planet. Sci. Lett.* **2003**, *215*, 57–72. [CrossRef]
62. de Meyer, C.M.; Baumgartner, L.P.; Beard, B.L.; Johnson, C.M. Rb–Sr ages from phengite inclusions in garnets from high pressure rocks of the Swiss Western Alps. *Earth Planet. Sci. Lett.* **2014**, *395*, 205–216. [CrossRef]
63. Skora, S.; Mahlen, N.J.; Johnson, C.M.; Baumgartner, L.P.; Lapen, T.J.; Beard, B.L.; Szilvagyi, E.T. Evidence for protracted prograde metamorphism followed by rapid exhumation of the Zermatt-Saas Fee ophiolite. *J. Metamorph. Geol.* **2015**, *33*, 711–734. [CrossRef]
64. Skora, S.; Lapen, T.J.; Baumgartner, L.P.; Johnson, C.M.; Hellebrand, E.; Mahlen, N.J. The duration of prograde garnet crystallization in the UHP eclogites at Lago di Cignana, Italy. *Earth Planet. Sci. Lett.* **2009**, *287*, 402–411. [CrossRef]
65. Bowtell, S.; Cliff, R.; Barnicoat, A. Sm-Nd isotopic evidence on the age of eclogitization in the Zermatt-Saas ophiolite. *J. Metamorph. Geol.* **1994**, *12*, 187–196. [CrossRef]
66. Rubatto, D.; Gebauer, D.; Fanning, M. Jurassic formation and Eocene subduction of the Zermatt-Saas-Fee ophiolites: implications for the geodynamic evolution of the Central and Western Alps. *Contrib. Mineral. Petrol.* **1998**, *132*, 269–287. [CrossRef]
67. Amato, J.M.; Johnson, C.M.; Baumgartner, L.P.; Beard, B.L. Rapid exhumation of the Zermatt-Saas ophiolite deduced from high-precision SmNd and RbSr geochronology. *Earth Planet. Sci. Lett.* **1999**, *171*, 425–438. [CrossRef]
68. Gouzu, C.; Itaya, T.; Hyodo, H.; Matsuda, T. Excess 40Ar-free phengite in ultrahigh-pressure metamorphic rocks from the Lago di Cignana area, Western Alps. *Lithos* **2006**, *92*, 418–430. [CrossRef]
69. Mahlen, N.J.; Johnson, C.M.; Baumgartner, L.P.; Lapen, T.J.; Skora, S.; Beard, B.L. The protracted subduction history and HP/UHP metamorphism of the Zermatt–Saas ophiolite, western Alps, as con- strained by Lu–Hf geochronology. In *EOS Transactions AGU Fall Meeting*; American Geophysical Union (AGU): Washington, DC, USA, 2006; pp. 11–15.
70. Dragovic, B.; Angiboust, S.; Tappa, M.J. Petrochronological close-up on the thermal structure of a paleo-subduction zone (W. Alps). *Earth Planet. Sci. Lett.* **2020**, *547*, 1–12. [CrossRef]
71. Hunziker, J.C.; Desmons, J.; Hurford, A.J. *Thirty-Two Years of Geochronological Work in the Central and Western Alps: A Review of Seven Maps*; Memoires de Geologie: Lausanne, Switzerland, 1992; Volume 13, p. 59.
72. Delaloye, M.; Desmons, J. K- Ar Radiometric Age Determinations of White Micas from the Piemont Zone, French-Italian Western Alps. *Contrib. Mineral. Petrol.* **1976**, *57*, 297–303.
73. Agard, P.; Monié, P.; Jolivet, L.; Goffé, B. Exhumation of the Schistes Lustrés complex: in situ laser probe 40Ar/39Ar constraints and implications for the Western Alps. *J. Metamorph. Geol.* **2002**, *20*, 599–618. [CrossRef]
74. Liewig, N.; Caron, J.M.; Clauer, N. Geochemical and K-Ar isotopic behaviour of alpine sheet silicates during polyphased deformation. *Tectonophysics* **1981**, *78*, 273–290. [CrossRef]

75. Bonhomme, M.G.; Saliot, P.; Pinault, Y. Interpretation of Potassium-Argon Isotopic Data Related to metamorphic Events in South-Western Alps. *Schweizerische Mineralogische und Petrographische Mitteilungen* **1980**, *60*, 81–98. [CrossRef]
76. Takeshita, H.; Shimoya, H.; Itaya, T. White mica K-Ar ages of blueschist-facies rocks from the Piemonte 'calc-schists' of the western Italian Alps. *Island Arc* **1994**, *3*, 151–162.
77. Takeshita, H.; Gouzu, C.; Itaya, T. Chemical Features of White Micas from the Piemonte Calc-schists, Western Alps and Implications for K-Ar Ages of Metamorphism. *Gondwana Res.* **2004**, *7*, 457–466. [CrossRef]
78. Caby, R.; Bonhomme, M.G. Whole-rock and fine fraction K-Ar isotopic study of radiolarites affected by the alpine metamorphism; evidence and consequences of excess argon 40. In Proceedings of the Fifth International Conference on Geochronology, Cosmochronology, Isotope Geology, Nikko, Japan, 27 June–2 July 1982; p. 42.
79. Liati, A.; Froitzheim, N.; Fanning, C.M. Jurassic ophiolites within the Valais domain of the Western and Central Alps: geochronological evidence for re-rifting of oceanic crust. *Contrib. Mineral. Petrol.* **2005**, *149*, 446–461. [CrossRef]
80. Herwartz, D.; Münker, C.; Scherer, E.E.; Nagel, T.J.; Pleuger, J.; Froitzheim, N. Lu-Hf garnet geochronology of eclogites from the Balma Unit (Pennine Alps): implications for Alpine paleotectonic reconstructions. *Swiss J. Geosci.* **2008**, *101*, 173–189. [CrossRef]
81. Duchene, S.; Lardeaux, J.M.; Albarede, F. Exhumation of eclogites: Insights from depth-time path analysis. *Tectonophysics* **1997**, *280*, 125–140. [CrossRef]
82. Rubatto, D.; Hermann, J. Zircon formation during fluid circulation in eclogites (Monviso, Western Alps): Implications for Zr and Hf budget in subduction zones. *Geochimica et Cosmochimica Acta* **2003**, *67*, 2173–2187. [CrossRef]
83. Cliff, R.; Barnicoat, A.; Inger, S. Early Tertiary eclogite facies metamorphism in the Monviso Ophiolite. *J. Metamorph. Geol.* **1998**, *16*, 447–455. [CrossRef]
84. Monié, P.; Philippot, P. 39Ar-40Ar evidence for mid-Eocene high-pressure metamorphism in the Monviso ophiolitic massif, Western Alps [Mise en évidence de l'âge éocène moyen du métamorphisme de haute-pression dans la nappe ophiolitique du Monviso (Alpes occidentales) par la méthode 39Ar-40Ar]. *Comptes Rendus - Academie des Sciences, Serie II* **1989**, *309*, 245–251.
85. Federico, L.; Capponi, G.; Crispini, L.; Scambelluri, M.; Villa, I. 39Ar/40Ar dating of high-pressure rocks from the Ligurian Alps: Evidence for a continuous subduction-exhumation cycle. *Earth Planet. Sci. Lett.* **2005**, *240*, 668–680. [CrossRef]
86. Compagnoni, R. The Sesia-Lanzo zone: high-pressure low-temperature metamorphism in the Austroalpine continental margin. *Rendiconti della Società Italiana di Mineralogia e Petrologia* **1977**, *33*, 335–374.
87. Gosso, G. Metamorphic evolution and fold history in the eclogite micaschists of the upper Gressoney valley (Sesia-Lanzo zone, Western Alps). *Rendiconti della Società Italiana di Mineralogia e Petrologia* **1977**, *33*, 389–407.
88. Babist, J.; Handy, M.R.; Konrad-Schmolke, M.; Hammerschmidt, K. Precollisional, multistage exhumation of subducted continental crust: The Sesia Zone, western Alps. *Tectonics* **2006**, *25*. [CrossRef]
89. Zucali, M.; Corti, L.; Delleani, F.; Zanoni, D.; Spalla, M.I. 3D reconstruction of fabric and metamorphic domains in a slice of continental crust involved in the Alpine subduction system: The example of Mt. Mucrone (Sesia-Lanzo Zone, Western Alps). *Int. J. Earth Sci.* **2020**. [CrossRef]
90. Zanoni, D.; Spalla, M.I.; Gosso, G. Structure and PT estimates across late-collisional plutons: constraints on the exhumation of western Alpine continental HP units. *Int. Geol. Rev.* **2010**, *52*, 1244–1267. [CrossRef]
91. Regis, D.; Rubatto, D.; Darling, J.; Cenki-Tok, B.; Zucali, M.; Engi, M. Multiple Metamorphic Stages within an Eclogite-facies Terrane (Sesia Zone, Western Alps) Revealed by Th-U-Pb Petrochronology. *J. Petrol.* **2014**, *55*, 1429–1456. [CrossRef]
92. Bertolani, M. La petrografia della cosidetta seconda zona kinzigitica nelle alte valli del Mastallone e del Sermenza (Val Sesia). *Rendiconti della Società Italiana di Mineralogia e Petrologia* **1971**, *27*, 368–391.
93. Dal Piaz, G.; Gosso, G.; Martinotti, G. La II zona diorito-kinzigitica tra la Val-Sesia e la Valle d'Ayas (Alpi Occidentali). *Memorie della Società Geologica Italiana* **1971**, *10*, 257–276.
94. Lardeaux, J.M.; Gosso, G.; Kienast, J.R.; Lombardo, B. Relations entre le métamorphisme et la déformation dans la zone Sesia-Lanzo (Alpes Occidentales) et le problème de l'é clogitisation de la croûte continentale. *Bulletin de la Societé Géologique de France* **1982**, *24*, 793–800.

95. Vuichard, J.P. Conditions P–T du métamorphisme anté-alpin dans la seconde zone diorito-kinzigitique (Zone Sesia-Lanzo, Alpes occidentales). *Schweizerische Mineralogische Und Petrographische Mitteilungen* **1987**, *67*, 257–271.
96. Compagnoni, R.; Maffeo, B. Jadeite bearing metagranites l.s. and related rocks in the Mount Mucrone Area (Sesia-Lanzo zone, Western Italian Alps). *Schweizerische Mineralogische Und Petrographische Mitteilungen* **1973**, *53*, 355–378.
97. Reinsch, D. Glaucophanites and eclogites from Val Chiusella, Sesia-Lanzo zone (Italian Alps). *Contrib. Mineral. Petrol.* **1979**, *70*, 257–266. [CrossRef]
98. Pognante, U.; Compagnoni, R.; Gosso, G. Micro-Mesostructural relationships in the continental eclogitic rocks of the Sesia-Lanzo Zone (Italian Western Alps): a record of subduction cycle. *Rendiconti della Società Italiana di Mineralogia e Petrologia* **1980**, *36*, 169–186.
99. Lardeaux, J.M. Evolution Tectono-Metamorphique de la Zone nord du Massif de Sesia-Lanzo (Alpes Occidentales): Un Exemple de éclogitisation de Croute Continentale. Ph.D. Thesis, Université de Paris VI, Paris, France, 1981.
100. Lardeaux, J.M.; Lombardo, B.; Gosso, G.; Kienast, J.R. Découverte de paragenèses à ferro-omphacites dans les orthogneiss de la zone Sesia-Lanzo septentrionale (Alpes Italiennes). *Compte Rendu Academie des Sciences Paris* **1983**, *296*, 453–456.
101. Pognante, U. Lawsonite, blueschist and eclogite formation in the southern Sesia Zone (Western Alps, Italy). *Eur. J. Mineral.* **1989**, *1*, 89–104. [CrossRef]
102. Venturini, G.; Martinotti, G.; Armando, G.; Barbero, M.; Hunziker, J.C. The central Sesia-Lanzo Zone (Western Italian Alps): new field observations and lithostratigrafic subdivisions. *Schweizerische Mineralogische Und Petrographische Mitteilungen* **1994**, *74*, 115–125.
103. Zucali, M.; Spalla, M.I.; Gosso, G.; Racchetti, S.; Zulbati, F. Prograde LWS-KY Transition During Subduction Of The Alpine Continental Crust Of The Sesia- Lanzo Zone: The Ivozio Complex. *J. Virtual Explor. Electron. Ed.* **2004**, *16*, 1–21. [CrossRef]
104. Rebay, G.; Messiga, B. Prograde metamorphic evolution and development of chloritoid-bearing eclogitic assemblages in subcontinental metagabbro (Sesia-Lanzo zone, Italy). *Lithos* **2007**, *98*, 275–291. [CrossRef]
105. Gosso, G.; Messiga, B.; Rebay, G.; Spalla, M.I. The interplay between deformation and metamorphism during eclogitization of amphibolites in the Sesia-Lanzo zone of the Western Alps. *Int. Geol. Rev.* **2010**, *51*, 1193–1219. [CrossRef]
106. Zanoni, D. Structural and petrographic analysis at the north-eastern margin of the Oligocene Traversella pluton (Internal Western Alps, Italy). *Italian J. Geosci.* **2010**, *129*, 51–68. [CrossRef]
107. Zucali, M.; Spalla, M.I. Prograde lawsonite during the flow of continental crust in the Alpine subduction: Strain vs. metamorphism partitioning, a field-analysis approach to infer 5 tectonometamorphic evolutions (Sesia-Lanzo Zone, Western Italian Alps). *J. Struct. Geol.* **2011**, *33*, 381–398. [CrossRef]
108. Giuntoli, F.; Engi, M. Internal geometry of the central Sesia Zone (Aosta Valley, Italy): HP tectonic assembly of continental slices. *Swiss J. Geosci.* **2016**, *109*, 445–471. [CrossRef]
109. Giuntoli, F.; Lanari, P.; Burn, M.; Kunz, B.E.; Engi, M. Deeply subducted continental fragments—Part 2: Insight from petrochronology in the central Sesia Zone (western Italian Alps). *Solid Earth* **2018**, *9*, 191–222. [CrossRef]
110. Pognante, U. Tectonic implications of lawsonite formation in the Sesia zone (Western Alps). *Tectonophysics* **1989**, *162*, 219–227. [CrossRef]
111. Spalla, M.I.; Zulbati, F. Structural and petrographic map of the southern Sesia-Lanzo Zone (Monte Soglio - Rocca Canavese, Western Alps, Italy). *Memorie di Scienze Geologiche, Padova* **2003**, *55*, 119–127.
112. Barnes, J.D.; Beltrando, M.; Lee, C.T.A.; Cisneros, M.; Loewy, S.; Chin, E. Geochemistry of Alpine serpentinites from rifting to subduction: A view across paleogeographic domains and metamorphic grade. *Chem. Geol.* **2014**, *389*, 29–47. [CrossRef]
113. Cantù, M.; Spaggiari, L.; Zucali, M.; Zanoni, D.; Spalla, M.I. Structural analysis of a subduction-related contact in southern Sesia-Lanzo Zone (Austroalpine Domain, Italian Western Alps). *J. Maps* **2016**, *12*, 22–35. [CrossRef]
114. Roda, M.; De Salvo, F.; Zucali, M.; Spalla, M.I. Structural and metamorphic evolution during tectonic mixing: is the Rocca Canavese Thrust Sheet (Italian Western Alps) a subduction-related mélange? *Italian J. Geosci.* **2018**, *137*, 311–329. [CrossRef]

115. Roda, M.; Zucali, M.; Regorda, A.; Spalla, M.I. Formation and evolution of a subduction-related mélange: The example of the Rocca Canavese Thrust Sheets (Western Alps). *GSA Bull.* **2020**, *132*, 884–896. [CrossRef]
116. Oberhänsli, R.; Hunziker, J.C.; Martinotti, G.; Stern, W.B. Geochemistry, geochronology and petrology of Monte Mucrone: An example of EO-alpine eclogitization of Permian granitoids in the Sesia-Lanzo Zone, Western Alps, Italy. *Chem. Geol.* **1985**, *52*, 165–184. [CrossRef]
117. Rubatto, D.; Gebauer, D.; Compagnoni, R. Dating of eclogite-facies zircons: The age of Alpine metamorphism in the Sesia-Lanzo Zone (Western Alps). *Earth Planet. Sci. Lett.* **1999**, *167*, 141–158. [CrossRef]
118. Cenki-Tok, B.; Oliot, E.; Rubatto, D.; Berger, A.; Engi, M.; Janots, E.; Thomsen, T.B.; Manzotti, P.; Regis, D.; Spandler, C.; et al. Preservation of Permian allanite within an Alpine eclogite facies shear zone at Mt Mucrone, Italy: Mechanical and chemical behavior of allanite during mylonitization. *Lithos* **2011**, *125*, 40–50. [CrossRef]
119. Halama, R.; Glodny, J.; Konrad-Schmolke, M.; Sudo, M. Rb-Sr and in situ 40Ar/39Ar dating of exhumation-related shearing and fluid-induced recrystallization in the Sesia zone (Western Alps, Italy). *Geosphere* **2018**, *14*, 1425–1450. [CrossRef]
120. Ji, W.Q.; Malusà, M.G.; Tiepolo, M.; Langone, A.; Zhao, L.; Wu, F.Y. Synchronous Periadriatic magmatism in the Western and Central Alps in the absence of slab breakoff. *Terra Nova* **2019**, *31*, 120–128. [CrossRef]
121. Pelletier, L.; Müntener, O. High-pressure metamorphism of the Lanzo peridotite and its oceanic cover, and some consequences for the Sesia-Lanzo zone (northwestern Italian Alps). *Lithos* **2006**, *90*, 111–130. [CrossRef]
122. Piccardo, G.B. The Lanzo Peridotite Massif, Italian Western Alps: Jurassic Rifting of the Ligurian Tethys. Geol. Soc. Lond. Spec. Publ. **2010**, *337*, 47–69. [CrossRef]
123. Scambelluri, M.; Pennacchioni, G.; Gilio, M.; Bestmann, M.; Plümper, O.; Nestola, F. Fossil intermediate-depth earthquakes in subducting slabs linked to differential stress release. *Nat. Geosci.* **2017**, *10*, 960–966. [CrossRef]
124. Aoki, T.; Ozawa, K.; Bodinier, J.L.; Boudier, F.; Sato, Y. Thermal and decompression history of the Lanzo Massif, northern Italy: Implications for the thermal structure near the lithosphere-asthenosphere boundary. *Lithos* **2020**, *372-373*, 105661. [CrossRef]
125. Rebay, G.; Spalla, M.I. Emplacement at granulite facies conditions of the Sesia-Lanzo metagabbros: An early record of Permian rifting? *Lithos* **2001**, *58*, 85–104. [CrossRef]
126. Rebay, G.; Riccardi, M.P.; Spalla, M.I. Fluid rock interactions as recorded by Cl-rich amphiboles from continental and oceanic crust of italian orogenic belts. *Periodico di Mineralogia* **2015**, *84*, 751–777. [CrossRef]
127. Ramsay, J. *Folding and Fracturing of Rocks*; McGraw-Hill: New York, NY, USA, 1967; p. 568. [CrossRef]
128. Whitney, D.L.; Evans, B.W. Abbreviations for names of rock-forming minerals. *Am. Mineral.* **2010**, *95*, 185–187. [CrossRef]
129. Padrón-Navarta, J.A.; Sánchez-Vizcaíno, V.L.; Hermann, J.; Connolly, J.A.; Garrido, C.J.; Gómez-Pugnaire, M.T.; Marchesi, C. Tschermak's substitution in antigorite and consequences for phase relations and water liberation in high-grade serpentinites. *Lithos* **2013**, *178*, 186–196. [CrossRef]
130. Droop, G.T.R. A general equation for estimating Fe 3+ concentrations in ferromagnesian silicates and oxides from microprobe analyses, using stoichiometric criteria. *Mineral. Mag.* **1987**, *51*, 431–435. [CrossRef]
131. De Hoog, J.C.; Gall, L.; Cornell, D.H. Trace-element geochemistry of mantle olivine and application to mantle petrogenesis and geothermobarometry. *Chem. Geol.* **2010**, *270*, 196–215. [CrossRef]
132. González-Jiménez, J.M.; Plissart, G.; Garrido, L.N.; Padrón-Navarta, J.A.; Aiglsperger, T.; Romero, R.; Marchesi, C.; Moreno-Abril, A.J.; Reich, M.; Barra, F.; et al. Titanian clinohumite and chondrodite in antigorite serpentinites from Central Chile: Evidence for deep and cold subduction. *Eur. J. Mineral.* **2017**, *29*, 959–970. [CrossRef]
133. Holland, T.J.B.; Powell, R. An internally consistent thermodynamic data set for phases of petrological interest. *J. Metamorph. Geol.* **1998**, *16*, 309–343. [CrossRef]
134. Powell, R.; Holland, T.; Worley, B. Calculating phase diagrams involving solid solutions via non-linear equations, with examples using THERMOCALC. *J. Metamorph. Geol.* **1998**, *16*, 577–588. [CrossRef]
135. Ernst, W.G.; Liou, J.G. High- and ultrahigh-pressure metamorphism: Past results and future prospects. *Am. Mineral.* **2008**, *93*, 1771–1786. [CrossRef]
136. Gerya, T.; Stöckhert, B.; Perchuk, A.L. Exhumation of high-pressure metamorphic rocks in a subduction channel: A numerical simulation. *Tectonics* **2002**, *21*, 1–15. [CrossRef]
137. Gerya, T.; Stöckhert, B. Two-dimensional numerical modeling of tectonic and metamorphic histories at active continental margins. *Int. J. Earth Sci. (Geol. Rundsch.)* **2005**, *95*, 250–274. [CrossRef]

138. Guillot, S.; Hattori, K.; Agard, P.; Schwartz, S.; Vidal, O. Exhumation Processes in Oceanic and Continental Subduction Contexts: A Review. In *Subduction Zone Dynamics*; Lallemand, S., Funiciello, F., Eds.; Springer-Verlag: Berlin/Heidelberg, Germany, 2009; pp. 175–204. [CrossRef]
139. Meda, M.; Marotta, A.M.; Spalla, M.I. The role of mantle hydration into the continental crust recycling in the wedge region. *Geol. Soc. Lond. Spec. Publ.* **2010**, *332*, 149–172. [CrossRef]
140. Roda, M.; Marotta, A.M.; Spalla, M.I. Numerical simulations of an ocean-continent convergent system: Influence of subduction geometry and mantle wedge hydration on crustal recycling. *Geochem. Geophys. Geosyst.* **2010**, *11*, 1–21. [CrossRef]
141. Platt, J.P. Dynamics of orogenic wedges and the uplift of high-pressure metamorphic rocks. *Geol. Soc. Am. Bull.* **1986**, *97*, 1037. [CrossRef]
142. Stöckhert, B.; Gerya, T. Pre-collisional high pressure metamorphism and nappe tectonics at active continental margins: A numerical simulation. *Terra Nova* **2005**, *17*, 102–110. [CrossRef]
143. Kronbichler, M.; Heister, T.; Bangerth, W. High accuracy mantle convection simulation through modern numerical methods. *Geophys. J. Int.* **2012**, *191*, 12–29. [CrossRef]
144. Heister, T.; Dannberg, J.; Gassmöller, R.; Bangerth, W. High accuracy mantle convection simulation through modern numerical methods—II: realistic models and problems. *Geophys. J. Int.* **2017**, *210*, 833–851. [CrossRef]
145. Rose, I.; Buffett, B.; Heister, T. Stability and accuracy of free surface time integration in viscous flows. *Phys. Earth Planet. Inter.* **2017**, *262*, 90–100. [CrossRef]
146. Bangerth, W.; Dannberg, J.; Gassmoeller, R.; Heister, T. ASPECT v2.2.0, 2020.
147. Afonso, J.C.; Ranalli, G. Crustal and mantle strengths in continental lithosphere: is the jelly sandwich model obsolete? *Tectonophysics* **2004**, *394*, 221–232. doi:10.1016/j.tecto.2004.08.006. [CrossRef]
148. Schoen, J. *Physical Properties of Rocks: A Workbook*; Elsevier B.V.: Amsterdam, The Netherlands, 2011; p. 494.
149. Ranalli, G. *Rheology of the Earth*; Springer: Amsterdam, The Netherlands, 1995; p. 414.
150. Wilks, K.R.; Carter, N.L. Rheology of some continental lower crustal rocks. *Tectonophysics* **1990**, *182*, 57–77. [CrossRef]
151. Hilairet, N.; Reynard, B.; Wang, Y.; Daniel, I.; Merkel, S.; Nishiyama, N.; Petitgirard, S. High-Pressure Creep of Serpentine, Interseismic Deformation, and Initiation of Subduction. *Science* **2007**, *318*, 1910–1912. [CrossRef]
152. Petersen, K.D.; Schiffer, C. Wilson cycle passive margins: Control of orogenic inheritance on continental breakup. *Gondwana Res.* **2016**, *39*, 131–144. [CrossRef]
153. Karato, S.i.; Wu, P. Rheology of the Upper Mantle: A Synthesis. *Science* **1993**, *260*, 771–778. [CrossRef]
154. Lardeaux, J.M.; Spalla, M.I. From granulites to eclogites in the Sesia zone (Italian Western Alps): A record of the opening and closure of the Piedmont ocean. *J. Metamorph. Geol.* **1991**, *9*, 35–59. [CrossRef]
155. Dal Piaz, G.V. History of tectonic interpretations of the Alps. *J. Geodyn.* **2001**, *32*, 99–114. [CrossRef]
156. Schuster, R.; Stüwe, K. Permian metamorphic event in the Alps. *Geology* **2008**, *36*, 603–606. [CrossRef]
157. Marotta, A.M.; Roda, M.; Conte, K.; Spalla, M.I. Thermo-mechanical numerical model of the transition from continental rifting to oceanic spreading: the case study of the Alpine Tethys. *Geol. Mag.* **2018**, *155*, 250–279. [CrossRef]
158. Roda, M.; Regorda, A.; Spalla, M.I.; Marotta, A.M. What drives Alpine Tethys opening? Clues from the review of geological data and model predictions. *Geol. J.* **2019**, *54*, 2646–2664. [CrossRef]
159. Festa, A.; Balestro, G.; Borghi, A.; De Caroli, S.; Succo, A. The role of structural inheritance in continental break-up and exhumation of Alpine Tethyan mantle (Canavese Zone, Western Alps). *Geosci. Front.* **2020**, *11*, 167–188. [CrossRef]
160. Korenaga, T.; Korenaga, J. Evolution of young oceanic lithosphere and the meaning of seafloor subsidence rate. *J. Geophys. Res. Solid Earth* **2016**, *121*, 6315–6332. [CrossRef]
161. Carlson, R.L.; Miller, D.J. A new assessment of the abundance of serpentinite in the oceanic crust. *Geophys. Res. Lett.* **1997**, *24*, 457–460. [CrossRef]
162. Juteau, T.; Maury, R. *The Oceanic Crust, from Accrection to Mantle Recycling*; Praxis Springer: London, UK, 1999; p. 402.
163. Christensen, N.I. Serpentinites, Peridotites, and Seismology. *Int. Geol. Rev.* **2004**, *46*, 795–816. [CrossRef]
164. Malvoisin, B.; Brunet, F.; Carlut, J.; Rouméjon, S.; Cannat, M. Serpentinization of oceanic peridotites: 2. Kinetics and processes of San Carlos olivine hydrothermal alteration. *J. Geophys. Res. Solid Earth* **2012**, *117*. [CrossRef]

165. Cannat, M.; Fontaine, F.; Escartín, J. Serpentinization and Associated Hydrogen And Methane Fluxes at Slow Spreading Ridges. In *Diversity of Hydrothermal Systems on Slow Spreading Ocean Ridges*; American Geophysical Union (AGU): Washington, DC, USA, 2013; pp. 241–264. [CrossRef]
166. Rüpke, L.H.; Hasenclever, J. Global rates of mantle serpentinization and H 2 production at oceanic transform faults in 3-D geodynamic models. *Geophys. Res. Lett.* **2017**, *44*, 6726–6734. [CrossRef]